

Skull-stripping induces shortcut learning in MRI-based Alzheimer's disease classification

Christian Tinauer^{1[0000-0003-4355-3898]}, Maximilian Sack^{1[0000-0002-1927-7953]}, Rudolf Stollberger^{2,3[0000-0002-4969-3878]}, Reinhold Schmidt^{1[0000-0002-6406-7584]}, Stefan Ropele^{1,3[0000-0002-5559-768X]}, and Christian Langkammer^{1,3[0000-0002-7097-9707]},
for the Alzheimer's Disease Neuroimaging Initiative*

¹ Department of Neurology, Medical University of Graz, 8036 Graz, Austria

{christian.tinauer, christian.langkammer}@medunigraz.at

<https://neuroimaging.at>

² Institute of Biomedical Imaging, Graz University of Technology, 8010 Graz, Austria

³ BioTechMed-Graz, 8010 Graz, Austria

Abstract.

Objectives. High classification accuracy of Alzheimer's disease (AD) from structural MRI has been achieved using deep neural networks, yet the specific image features contributing to these decisions remain unclear. In this study, the contributions of T1-weighted (T1w) gray-white matter texture, volumetric information, and preprocessing -particularly skull-stripping- were systematically assessed.

Methods. A dataset of 990 matched T1w MRIs from AD patients and cognitively normal controls from the ADNI database were used. Preprocessing was varied through skull-stripping and intensity binarization to isolate texture and shape contributions. A 3D convolutional neural network was trained on each configuration, and classification performance was compared using exact McNemar tests with discrete Bonferroni-Holm correction. Feature relevance was analyzed using Layer-wise Relevance Propagation, image similarity metrics, and spectral clustering of relevance maps.

Results. Despite substantial differences in image content, classification accuracy, sensitivity, and specificity remained stable across preprocessing conditions. Models trained on binarized images preserved performance, indicating minimal reliance on gray-white matter texture. Instead, volumetric features -particularly brain contours introduced through skull-stripping- were consistently used by the models.

Conclusions. This behavior reflects a shortcut learning phenomenon, where preprocessing artifacts act as potentially unintended cues. The resulting Clever Hans effect emphasizes the critical importance of interpretability tools to reveal hidden biases and to ensure robust and trustworthy deep learning in medical imaging.

Relevance Statement. We investigated the mechanisms underlying deep learning-based disease classification using a widely utilized Alzheimer's disease dataset and our findings reveal

*Data used in preparation of this article were obtained from the Alzheimer's Disease Neuroimaging Initiative (ADNI) database (<https://adni.loni.usc.edu>). As such, the investigators within the ADNI contributed to the design and implementation of ADNI and/or provided data but did not participate in analysis or writing of this report. A complete listing of ADNI investigators can be found at: https://adni.loni.usc.edu/wp-content/uploads/how_to_apply/ADNI_Acknowledgement_List.pdf

a reliance on features induced through skull-stripping, highlighting the need for careful pre-processing to ensure clinically relevant and interpretable models.

Key Points.

- Demonstrates that shortcut learning is induced by skull-stripping applied to T1-weighted MRIs.
- Uses McNemar tests, explainable deep learning and spectral clustering to estimate the bias.
- Highlights the importance of understanding the dataset, image preprocessing and deep learning model, for interpretation and validation.

Keywords: Shortcut learning · Preprocessing bias · Alzheimer's disease · Explainable deep learning

1 Introduction

Alzheimer's disease (AD) is the most common form of dementia, accounting for 60-70% of cases [34] and with over 55 million people worldwide living with some form of dementia, it poses a substantial burden on healthcare systems, caregivers, and families [1]. However, *in vivo* diagnosis remains challenging due to the overlap of clinical symptoms with other conditions, resulting in relatively low diagnostic accuracy (71-87% sensitivity and 44-71% specificity) [3].

In addition to clinical and neuropsychological assessments, medical imaging is employed to improve diagnostic accuracy. Positron emission tomography (PET) imaging with amyloid and tau protein ligands, combined with magnetic resonance imaging (MRI), has become a valuable tool in AD diagnosis [14]. Yet, AD is characterized by a prolonged prodromal and asymptomatic inflammatory phase, during which PET imaging is unsuitable for predicting disease onset in healthy populations. Since pathological changes in AD begin decades before clinical symptoms appear, MRI holds promise for identifying early biomarkers in a broad population. Currently, brain volumetry [38], particularly hippocampal atrophy [17], is widely used as an imaging marker for differential diagnosis and in interventional studies.

In recent years, convolutional neural networks (CNNs) have emerged as the state-of-the-art method for AD classification using structural T1-weighted (T1w) MRI scans [47]. These networks learn image features directly during the training process, eliminating the need for manual feature selection. Despite their advantages, CNN models and the features they extract are often difficult for humans to interpret, earning them the reputation of being "black boxes" [11].

To address this issue, interpretability methods like heatmaping have been introduced [37]. One notable technique is Layer-wise Relevance Propagation (LRP) [2], which highlights input features driving model decisions. The importance of such tools is illustrated by cases like [24], where a model identified horses based on watermarks rather than the animals - an instance of the Clever Hans effect [6,46]. This term, drawn from a horse once thought to perform arithmetic but later shown to respond to subtle cues [33], exemplifies shortcut learning: the exploitation of spurious correlations over meaningful patterns [16].

In AD classification, interpretability research has shown that preprocessing steps can shape both

performance and learned features [42]. We hypothesize that skull-stripping, a common step, may introduce unintended cues and lead models to overlook more relevant AD-specific markers, such as structural atrophy and gray-white matter contrast changes [9].

In this study, we combined deep learning and heatmap explainability techniques to evaluate the performance and learned features of CNNs trained on different input configurations. Specifically, we trained identical CNN architectures on full T1w images from the Alzheimer's Disease Neuroimaging Initiative (ADNI) dataset, their skull-stripped counterparts, and three differently binarized versions of these two preprocessing approaches, creating a total of eight model configurations. We first analyzed performance metrics for significant differences, assessed structural similarities between LRP-based heatmaps, and investigated the spatial distribution of heatmap relevance to examine whether preprocessing introduced unintended cues [45].

2 Materials and Methods

2.1 Imaging Data

Using MR image metadata from the ADNI database (<https://adni.loni.usc.edu>), we created a subset of images with clinically available and consistent properties. The final search criteria were: Phase = ADNI 2, Acquisition Plane = SAGITTAL, Field Strength = 3.0 Tesla, Pixel Spacing XY = [1.0 mm, 1.1 mm], Slice Thickness = 1.2 mm, and Weighting = T1. These criteria resulted in 1,042 images for the AD group and 2,227 images for the normal control (NC) group. This ensured that patients and controls were scanned using a consistent MRI protocol at 3 Tesla across multiple scanner vendors and sites. Supplementary Table 4 and Supplementary Table 5 in **Supplementary Material 1** provide an overview of the distribution of images across sites, vendors, imaging protocols, and research groups.

2.2 Research Groups

We retrospectively selected 990 MR images from 159 patients with AD and 990 MR images from 201 propensity-logit-matched NCs that were propensity-logit-matched using age and sex as covariates from the preselected image data subset [22]. Supplementary Figure 4 in **Supplementary Material 1** details effect sizes before and after matching. Table 1 shows the demographics of the selection. Data were split into training, validation, and test sets (ratio 70:15:15), ensuring that all scans from a given individual were included in the same set. To maintain consistent class distribution, the final sets were created by combining data from both cohorts.

2.3 Preprocessing

Raw T1w images were reoriented to standard space using FSL-REORIENT2STD [20], cropped to a $160 \times 240 \times 256$ matrix size, bias field corrected using N4 [44], and non-linearly registered to the MNI152 template via FSL-FNIRT [20]. Intensity values were normalized to the white matter peak of the brain tissue histogram (196 bins). The outputs of this preprocessing pipeline are referred to as “aligned” images. Individual brain masks were generated in native image space using SIENAX from FSL [39] and warped to the aligned images to create the “skull-stripped” images. Binary masks preserving shape information were derived using manually selected thresholds of 13.75%,

Table 1: Summary of subject demographics at baseline for ADNI. Note. Values are presented as mean \pm SD [range]. M: male, F: female, MMSE: mini-mental state examination, CDR: global clinical dementia rating, APOE: Apolipoprotein E status, Education in years, n/a: no value available.

Subjects	Images	Age	Gender	MMSE	CDR	APOE	Education
NC 201	990	75.1 \pm 7.1 [56.3, 95.8]	102 M/ 99 F	28.9 \pm 1.2 [24.0, 30.0] n/a: 16	0.0: 171; 0.5: 13; n/a: 17	$\epsilon 2/\epsilon 2$: 1; $\epsilon 2/\epsilon 3$: 20; $\epsilon 2/\epsilon 4$: 1; $\epsilon 3/\epsilon 3$: 112; $\epsilon 3/\epsilon 4$: 49; $\epsilon 4/\epsilon 4$: 5; n/a: 13	16.7 \pm 2.5 [12.0, 20.0] n/a: 0
AD 159	990	75.3 \pm 7.9 [55.7, 91.5]	91 M/ 68 F	22.0 \pm 3.8 [4.0, 30.0] n/a: 48	0.5: 35; 1.0: 67; 2.0: 9; n/a: 48	$\epsilon 2/\epsilon 2$: 1; $\epsilon 2/\epsilon 3$: 5; $\epsilon 2/\epsilon 4$: 2; $\epsilon 3/\epsilon 3$: 41; $\epsilon 3/\epsilon 4$: 68; $\epsilon 4/\epsilon 4$: 29; n/a: 13	15.7 \pm 2.7 [9.0, 20.0] n/a: 0

27.5%, and 41.25% of the white matter peak of the brain tissue histogram and the aligned images. These binary masks were also combined with skull-stripped preprocessing, resulting in eight total setups, as illustrated in Figure 1. Supplementary Figure 5 in [Supplementary Material 1](#) illustrates that thresholds were selected to preserve meaningful atrophy patterns by comparing residual voxels with individual brain masks.

2.4 Standard classification network

We utilized a conventional 3D subject-level classifier network as described in [\[47\]](#). However, because the number of trainable parameters (42 million) relative to the dataset size (1980 images) is high, the network is prone to overfitting. To address this, we reduced the number and size of the convolutional and fully connected layers until the network no longer overfit the training data and the validation accuracy ceased to improve. See [Supplementary Material 2](#) for loss and performance curves. Batch normalization layers did not influence the network’s performance and were therefore omitted. Additionally, we replaced max pooling layers with convolutional layers using striding, as tested in [\[40\]](#). This modification improves the interpretability of the network [\[32\]](#). Dropout was not applied in the network. To further enhance interpretability, all biases in the classifier were constrained to be non-positive, which helped sparsify the network activations [\[32\]](#).

The final 3D classifier network, as shown in Figure 2, consists of a single convolutional layer (kernel size: $3 \times 3 \times 3$, 8 channels) combined with a down-convolutional layer (kernel size: $3 \times 3 \times 3$, 8 channels, striding: 2) as its primary building block. The network stacks four of these main building blocks, followed by two fully connected layers (with 16 and 2 units, respectively), resulting in a to-

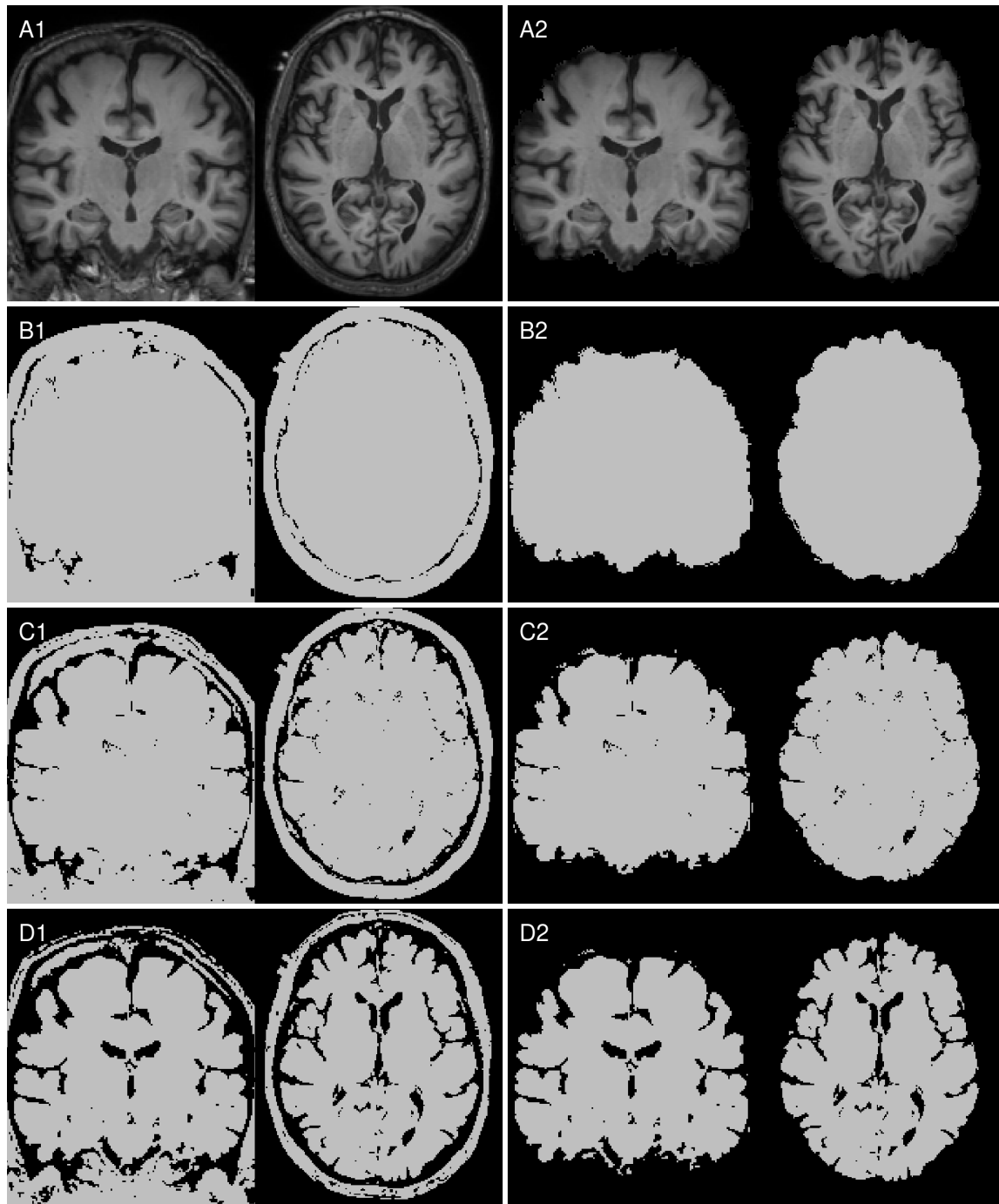


Fig. 1: Input image setups: Left column with (A1) aligned T1w MRI, identical binarized T1w images with the manually selected threshold levels (B1) 13.75%, (C1) 27.50% (C1) and (D1) 41.25%, and in the right column the corresponding skull-stripped versions (A2, B2, C2, D2).

tal of 0.3 million trainable parameters. Each layer is followed by a Rectified Linear Unit activation function, except for the output layer, which employs a Softmax activation.

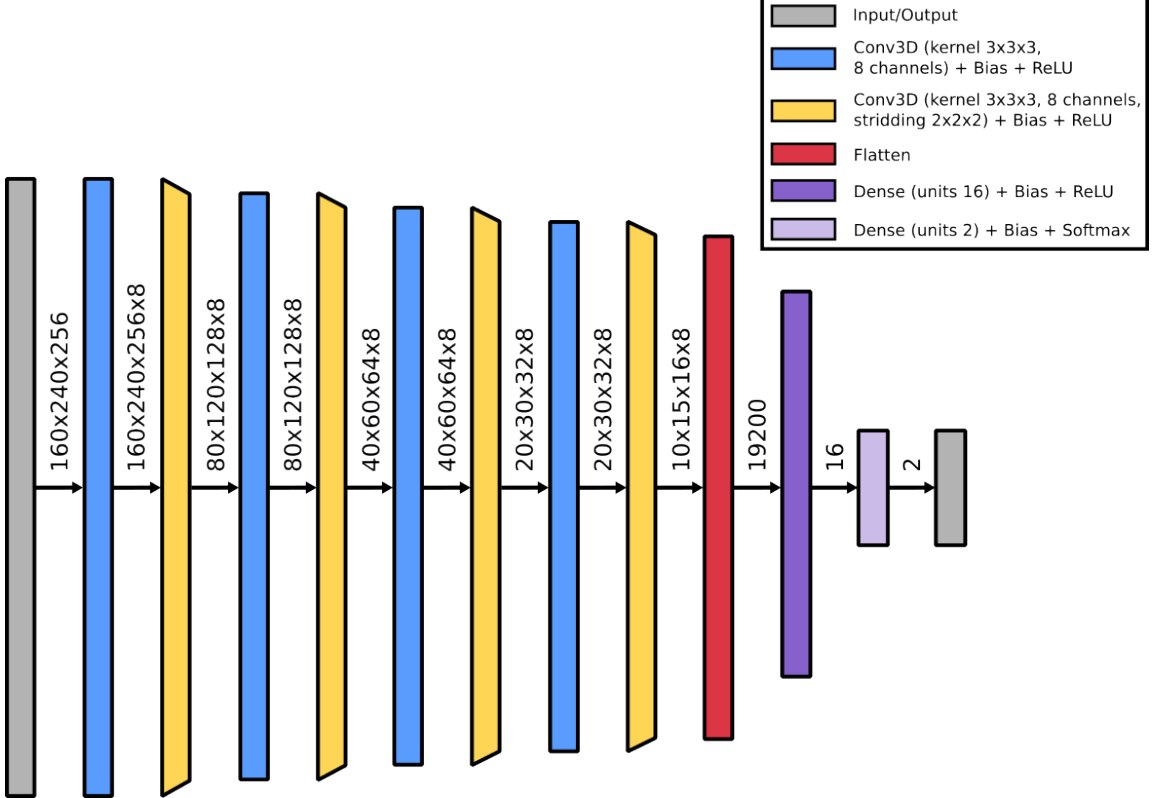


Fig. 2: Structure of the 3D classifier network. Dimensionalities between layers are the tensor sizes.

2.5 Training

Models were trained on aligned images, skull-stripped images, and their binarized counterparts. Training was performed using the Adam optimizer [21] for 30 epochs with a batch size of 20 using three independent network weights initializations [7] minimizing the binary cross entropy loss. Each data sampling was trained with all three initializations.

2.6 Heatmapping and relevance-weighted heatmap presentation

Heatmaps were created using the LRP method with $\alpha=1.0$ and $\beta=0.0$, as described in [2]. Each voxel is attributed a relevance score (R). To analyze relevance heatmaps, we qualitatively examined individual maps and calculated mean heatmaps for each configuration. For each mean heatmap,

we generated a histogram of relevance values. Starting from the bin with the highest relevance, bin contents were iteratively summed until 40% of the total relevance was included. The lower bound of the final bin was used as the lower threshold for windowing the mean heatmap. All heatmaps presented in this study are overlaid on the MNI152 1 mm template and windowed to display the top 40% of relevance.

2.7 Random sampling

For each data sampling (10 samplings) and each network weight initialization (3 initializations), we retrained the network, resulting in 30 training sessions for each input image configuration [8]. Non-converging training sessions were excluded from further analysis. From the remaining sessions, the best-performing run based on validation accuracy was selected to create the mean heatmaps.

2.8 Statistical analysis

We calculated performance metrics, including accuracy, sensitivity, specificity, and the area under the receiver operating characteristic curve (AUC), for all model configurations. Results are reported as mean values, standard deviations, and 95% confidence intervals. The model trained on skull-stripped T1w images (see A2 in Figure 1) was designated as the reference model for statistical comparisons. Exact McNemar tests were performed to compare accuracy, sensitivity, and specificity between the reference model and each alternative model for each session run (combination of data sampling and weight initialization), provided both runs were available [12]. To account for multiple comparisons, we applied the discrete Bonferroni-Holm correction, a statistical method suitable for adjusting comparisons involving overlapping data splits [48].

2.9 Heatmap similarity analysis

To evaluate heatmap similarities, we compared the best-performing run of the reference model with the corresponding runs (same data sampling and weight initialization) of each alternative model using structural image similarity measures. Before comparison heatmaps were normalized to min-max. Voxel-wise similarity was assessed with the root mean square error (RMSE), while global trends and overall similarity were evaluated using the Pearson correlation coefficient. Both global and localized patterns were analyzed with the mean structural similarity index measure (MSSIM) and Earth Mover’s Distance (EMD). Additionally, binarized heatmaps highlighting the top 40% and top 10% relevance values were compared using the Intersection over Union (IoU) metric.

3 Results

The following sections present quantitative performance results across setups, followed by an analysis of CNN-extracted features using LRP and image similarity metrics.

3.1 Model performances

Table 2 provides the results of the accuracy, sensitivity, specificity, and AUC for all configurations in the random sampling setup. Performance metrics were evaluated across non-excluded training

sessions for each model configuration.

Using an alpha level of .05 and discrete Bonferroni-Holm correction for multiple exact McNemar tests, comparisons between the reference model (A2, skull-stripped, no binarization) and alternative configurations -including binarized skull-stripped images at thresholds of 13.75% (B2, 8 significant differences), 27.50% (C2, 1 significant difference), and 41.25% (D2, 4 significant differences) as well as aligned images binarized at 41.25% (D1, 7 significant differences)- revealed little to no evidence for significant differences in accuracy, sensitivity, and specificity. 120 of 600 total comparisons remained significant after correction for multiple testing. See [Supplementary Table 6](#) in [Supplementary Material 3](#) for significant differences in model comparisons.

Aligned images with binarization thresholds 13.75% and 27.50% (B1, C1) performed comparably to aligned T1w images without binarization (A1). Similarly, skull-stripped images with binarization (B2, C2, D2) and aligned images binarized at 41.25% (D1) exhibited comparable performance to skull-stripped images without binarization (A2) while outperforming other aligned image configurations.

Additionally, model performances were tested on our local, non-public datasets. See [Supplementary Material 4](#) for results.

Table 2: Summary of performance metrics of all configurations. Note. AUC = area under receiver operating characteristics curve. Values between [and] show the 95% confidence interval.

Input images	Id	Binarizer	Accuracy	Sensitivity	Specificity	AUC
Aligned T1w	A1	None	71.12±5.01% [61.34%, 82.52%]	67.47±9.90% [51.66%, 85.94%]	74.76±7.07% [62.03%, 85.45%]	0.71±0.05 [0.62, 0.83]
	B1	13.75%	62.51±5.45% [53.39%, 72.09%]	62.26±9.48% [47.70%, 84.93%]	62.79±8.35% [46.56%, 74.42%]	0.63±0.054 [0.53, 0.72]
	C1	27.50%	72.74±5.49% [61.41%, 82.11%]	71.37±9.10% [56.86%, 88.87%]	74.15±9.94% [51.67%, 88.37%]	0.73±0.055 [0.61, 0.82]
	D1	41.25%	77.95±4.57% [70.90%, 86.34%]	76.74±9.41% [60.10%, 94.56%]	79.15±6.80% [64.54%, 89.56%]	0.78±0.045 [0.71, 0.86]
Skull-stripped T1w	A2	None	81.63±3.77% [74.36%, 88.01%]	81.22±6.94% [69.59%, 93.15%]	82.11±7.92% [65.50%, 93.60%]	0.82±0.037 [0.74, 0.88]
	B2	13.75%	78.12±4.63% [70.79%, 85.79%]	76.83±7.03% [62.65%, 87.05%]	79.40±6.76% [65.53%, 89.91%]	0.78±0.046 [0.71, 0.86]
	C2	27.50%	79.57±3.92% [73.46%, 86.45%]	78.32±7.74% [66.79%, 93.87%]	80.92±7.71% [67.53%, 91.95%]	0.80±0.039 [0.74, 0.86]
	D2	41.25%	81.56±4.63% [72.31%, 88.67%]	79.69±9.42% [62.59%, 96.48%]	83.50±6.77% [72.48%, 96.29%]	0.82±0.046 [0.72, 0.89]

3.2 Feature similarities

Figure 3 shows mean heatmaps for classification decisions on test images. Skull-stripping enhances classification accuracy, while mean heatmaps from binarized inputs closely resemble those from

non-binarized inputs.

Heatmaps from the skull-stripped model (A2) serve as the reference for structural heatmap comparisons in Table 3. Skull-stripped binarization (B2, C2, D2) shows lower voxel-wise dissimilarity (RMSE), higher global similarity (Pearson Correlation), and improved localized similarity (MSSIM, EMD) compared to the aligned versions (A1, B1, C1, D1). Among the binarized models, skull-stripped-binarization-13.75% (B2) demonstrates the highest overall structural similarity (RMSE, Pearson Correlation, MSSIM, EMD) with the reference (A2), while skull-stripped-binarization-27.50% exhibits the strongest regional overlap with the reference. These results emphasize the dominant role of volumetric features over T1w contrast variations. Features similarities and model misclassification analysis were furthermore done using spectral clustering [24,27] and t-distributed stochastic neighbor embedding [28]. See [Supplementary Material 5](#) for an introduction and results.

Table 3: Summary of heatmap similarity metrics for all configurations compared to the reference model (A2). Note. Values between [] show the 95% confidence interval. Bin. = Binarizer, RMSE = root mean square error, Corr. = Correlation, MSSIM = mean structural similarity index measure, EMD = Earth Mover's Distance, IoU = Intersection over Union, R = Relevance.

Input images	Id	Bin. %	RMSE	Pearson Corr.	MSSIM	EMD	IoU Top 40% R	IoU Top 10% R
Aligned T1w	A1	None	10.78±3.76 [5.98, 21.47]	0.13±0.04 [0.06, 0.21]	0.25±0.08 [0.12, 0.42]	8.44±3.25 [3.99, 17.48]	0.06±0.02 [0.02, 0.11]	0.01±0.01 [0.00, 0.03]
	B1	13.75	3.85±0.87 [2.25, 5.48]	0.08±0.03 [0.03, 0.15]	0.87±0.04 [0.78, 0.94]	0.50±0.29 [0.14, 1.29]	0.02±0.01 [0.01, 0.04]	0.00±0.00 [0.00, 0.01]
	C1	27.50	4.77±0.96 [3.07, 6.64]	0.18±0.05 [0.08, 0.26]	0.83±0.04 [0.74, 0.89]	0.71±0.45 [0.11, 1.71]	0.07±0.02 [0.03, 0.10]	0.01±0.01 [0.00, 0.02]
	D1	41.25	6.17±1.15 [3.98, 8.34]	0.23±0.05 [0.13, 0.30]	0.72±0.06 [0.62, 0.83]	1.61±0.62 [0.54, 2.75]	0.10±0.02 [0.05, 0.14]	0.01±0.01 [0.00, 0.03]
Skull-stripped T1w	A2	None	0.00±0.00	1.00±0.00	1.00±0.00	0.00±0.00	1.00±0.00	1.00±0.00
	B2	13.75	2.79±0.49 [1.97, 3.79]	0.58±0.07 [0.44, 0.69]	0.91±0.03 [0.82, 0.96]	0.39±0.25 [0.12, 1.05]	0.24±0.06 [0.13, 0.35]	0.15±0.03 [0.08, 0.21]
	C2	27.50	3.54±0.61 [2.45, 4.85]	0.56±0.07 [0.39, 0.67]	0.86±0.04 [0.78, 0.92]	0.73±0.44 [0.13, 1.67]	0.31±0.05 [0.20, 0.37]	0.17±0.03 [0.10, 0.24]
	D2	41.25	3.72±0.59 [2.69, 4.96]	0.51±0.08 [0.33, 0.65]	0.80±0.05 [0.68, 0.89]	1.01±0.50 [0.23, 2.12]	0.26±0.03 [0.18, 0.31]	0.16±0.04 [0.09, 0.22]

4 Discussion

Previous studies using T1w MRI for AD classification have reported strong CNN performance but often failed to clarify which image features -such as volumetric patterns, signal textures, or pre-processing artifacts- drive model decisions [42,5,36]. This lack of interpretability raises concerns about spurious correlations and shortcut learning. We address this gap through a systematic analysis using 1,980 T1w MR images from a widely used AD dataset. Applying explainable deep learning, McNemar-based model comparisons, and spectral clustering of LRP heatmaps, we disentangled the contributions of intensity and anatomical information. Texture removal via image binarization

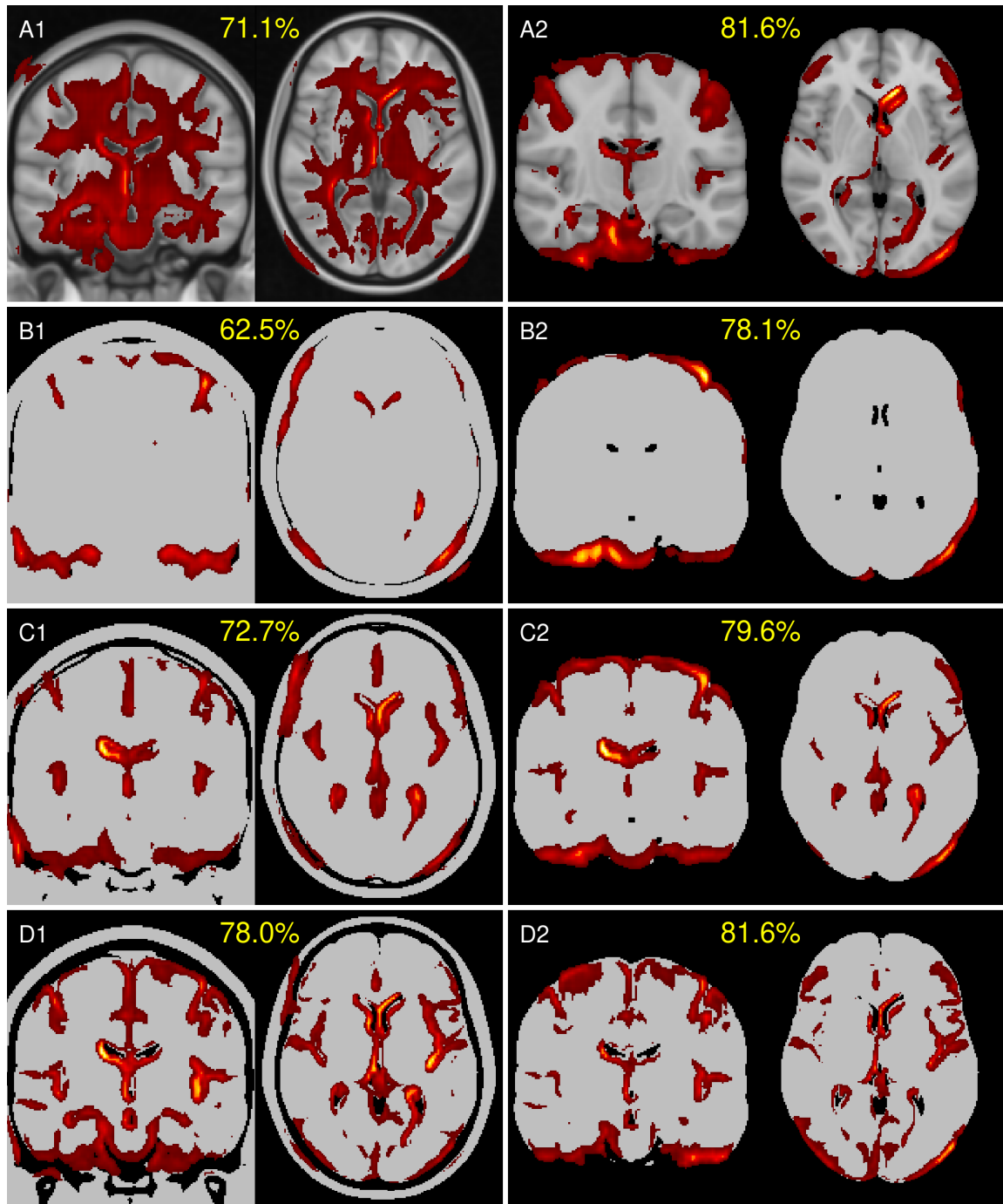


Fig. 3: Mean heatmaps from test images: Left column with (A1) aligned T1w MRI, identical binarized T1w image with threshold levels (B1) 13.75%, (C1) 27.50% (C1) and (D1) 41.25%, and right column with corresponding skull-stripped versions (A2, B2, C2, D2). The mean accuracies of the models are shown in yellow.

further isolated structural cues. Our analysis reveals a bias: CNNs rely heavily on volume-based features rather than biologically specific microstructural changes. These findings highlight the need for rigorous validation of AI tools and a deeper understanding of how dataset properties, preprocessing, and model behavior interact - an integrative perspective still lacking in the field.

To enable robust and unbiased evaluation, we curated a dataset with high inter-class image similarity and balanced class proportions [47]. We then applied one-to-one matching by sex and age to reduce covariate-driven influences, aiming to minimize confounders and ensure models focused on AD-related structural and contrast changes [9,25].

All models used non-linear registration to align MRIs to MNI152 space, accounting for individual anatomical variation. However, this does not fully correct for atrophy, which varies regionally in AD, especially in the hippocampus and cortical gray matter [42].

Skull-stripping, our reference preprocessing step, is widely used in AD classification and supported by heatmap-based studies showing improved accuracy in AD [5], dementia [25], multiple sclerosis [15], and brain age prediction [18,19,13].

Heatmaps generated in this study corroborate these findings, with relevance predominantly concentrated at the tissue boundary. To further probe the contribution of volumetric features, we removed tissue contrast entirely through binarization, isolating atrophic and structural features for analysis.

We investigated three binarization levels, each aligned with the white matter intensity peak of the image, as depicted in Figure 1. These levels, although chosen arbitrarily, retained differing proportions of anatomical structures, capturing distinct aspects of atrophy, including ventricular enlargement, hippocampal shrinking and cerebellum morphology. As CNNs seem to focus on high-contrast regions [15,31], these binarization levels allowed us to systematically dissect how different volumetric and structural features influenced model predictions.

Performance metrics, summarized in Table 2, reveal that removing gray-white matter contrast while retaining skull-stripping has little to no effect on model performance. Statistical analyses using exact McNemar tests, adjusted with discrete Bonferroni-Holm correction ($\alpha = .05$), revealed minimal evidence of significant differences in accuracy, sensitivity, and specificity across configurations when compared to the reference model. Specifically, skull-stripped and binarized models at thresholds of 13.75%, 27.50%, and 41.25%, as well as aligned images binarized at 41.25%, showed fewer than 10% of comparisons with significant differences. This suggests that volumetric information is sufficient for achieving high classification accuracy in CNN-based AD classification, with minimal contribution from gray-white texture variations.

Given the consistent model performances across configurations, we examined structural image similarities using similarity metrics applied on heatmaps, shown in Table 3. Surprisingly, the model trained with binarization at 13.75% (B2) -which retains the most tissue within the brain mask-exhibited the highest similarity to the reference model (A2) across global (RMSE, Pearson correlation) and localized (MSSIM, EMD) similarity metrics. This indicates that the key volumetric and morphological features driving classification are predominantly encoded in the brain mask's volume and shape.

Furthermore, starting at binarization-27.50% (C1, C2), models began to incorporate additional regions such as the ventricles, with binarization at 41.25% (D1, D2) capturing also hippocampal features. Notably, the highest overlaps between reference and binarized models were observed at 27.50% (C2), as indicated by intersection-over-union metrics. This suggests that contrast in ventricular regions in the reference model provides sufficient signal for the model to identify disease-relevant patterns.

Overall is the classification performance of the models driven by high contrast variations, either given by brain structures like the ventricular system and the hippocampi, or by being introduced artificially through image preprocessing. Multi-center studies have repeatedly shown that scanner vendor, acquisition protocol, and preprocessing pipeline systematically alter radiomic and image features, and consequently classifier behavior [23,4]. Effects can persist even after harmonization if applied improperly [26,30].

Drawing parallels to the Clever Hans effect -where unintended cues in the experimental setup were inadvertently learned- we observed a similar phenomenon in deep learning-based AD classification. Preprocessing, particularly skull-stripping in T1w imaging, is crucial for achieving state-of-the-art performance [47,5,25,13], as demonstrated by the inferior results of model A1 (aligned, no binarization) compared to A2 (skull-stripped, no binarization). However, when combined with a CNN, this preprocessing acts as an interviewer effect, steering the model toward artificially introduced yet well-established features like volumetry. This underscores the need for careful control of preprocessing artifacts [42] and suggests that quantitative MRI parameter maps [41,43,29] or model regularization [42] could offer a more robust alternative by minimizing reliance on such artificial cues.

4.1 Limitations

This study has its limitations. First, while the dataset is large, representative, and carefully crafted, it is derived solely from the ADNI database. However, the final models were tested on our local, nonpublic datasets. Second, our analysis primarily examines T1w images, preprocessing strategies, their impact on classification performance, and the features extracted using heatmaps. Third, the CNN architecture was intentionally simplified to control overfitting and was optimized for the reference model (skull-stripped, no binarization) by systematically reducing trainable parameters and complexity, alongside hyperparameter tuning. Although the final architecture achieved performance metrics comparable to existing literature, applying the same setup across experiments aimed to minimize bias but may not eliminate it entirely. It remains to be investigated whether similar effects would arise in more complex 3D architectures. However, we expect that such models would also be susceptible to the bias estimated in this study. Lastly, while heatmaps and similarity metrics were effective for feature interpretation, they may not fully capture the intricate interactions between features learned by the models.

4.2 Conclusion

Our findings uncover a shortcut learning effect in deep learning-driven AD classification, demonstrating that models predominantly rely on volumetric features rather than microstructural changes

in gray- and white matter. This highlights the critical need to evaluate data selection and preprocessing workflows to distinguish between artifacts and true disease-specific patterns, ensuring clinical relevance.

The implications of this work extend beyond AD classification, urging to adopt robust strategies for disentangling artifacts from meaningful features in deep learning workflows. Model validation pipelines should routinely test model sensitivity to preprocessing variations and data handling choices before clinical deployment. Future studies should incorporate quantitative MRI parameters, such as T1, R2*, or QSM, to provide insights into disease pathology and enhance model interpretability and generalizability. By addressing these challenges, the field can advance toward more reliable and clinically actionable applications of AI in neuroimaging.

Data and Code Availability. The code and the image ids (ADNI images) used in this study are available under <https://github.com/christiantinauer/binADNI>. The MR images from our local datasets are not publicly available. Formal data sharing requests to the corresponding authors will be considered.

Ethics Statement. Data used in this study were obtained from the Alzheimer's Disease Neuroimaging Initiative (ADNI) database (<https://adni.loni.usc.edu>). The ADNI study was conducted in accordance with the ethical standards of each participating institution's Institutional Review Board and with the 1964 Helsinki declaration and its later amendments. Written informed consent was obtained from all participants or their authorized representatives at the time of enrollment.

The current study involved only secondary analyses of fully de-identified data provided by ADNI, and no additional ethical approval was required. All analyses were conducted in accordance with the ADNI Data Use Agreement.

Additionally, this study used data acquired in local studies approved by the ethics committee of the Medical University of Graz (IRB00002556) and signed informed consent was obtained from all study participants or their caregivers. The trial protocol for this prospective study was registered at the National Library of Medicine (trial identification number: NCT02752750). All methods were performed in accordance with the relevant guidelines and regulations.

Funding. This study was funded by the Austrian Science Fund (FWF grant numbers: P30134, P35887).

Declaration of Competing Interest. The authors declare no competing interests.

Acknowledgments. We thank Lukas Pirpamer for the feedback provided during the creation of this manuscript.

Data collection and sharing for this project was funded by the Alzheimer's Disease Neuroimaging Initiative (ADNI) (National Institutes of Health Grant U01 AG024904) and DOD ADNI (Department of Defense award number W81XWH-12-2-0012). ADNI is funded by the National Institute on Aging, the National Institute of Biomedical Imaging and Bioengineering, and through generous contributions from the following: AbbVie, Alzheimer's Association; Alzheimer's Drug Discovery Foundation; Araclon Biotech; BioClinica, Inc.; Biogen; Bristol-Myers Squibb Company; CereSpir, Inc.; Cogstate; Eisai Inc.; Elan Pharmaceuticals, Inc.; Eli Lilly and Company; EuroImmun; F. Hoffmann-La Roche Ltd and its affiliated company Genentech, Inc.; Fujirebio; GE Healthcare; IXICO Ltd.; Janssen Alzheimer Immunotherapy Research & Development, LLC.; Johnson & Johnson Pharmaceutical Research & Development LLC.; Lumosity; Lundbeck; Merck & Co., Inc.; Meso Scale Diagnostics, LLC.; NeuroRx Research; Neurotrack Technologies; Novartis Pharmaceuticals Corporation; Pfizer Inc.; Piramal Imaging; Servier; Takeda Pharmaceutical Company; and Transition

Therapeutics. The Canadian Institutes of Health Research is providing funds to support ADNI clinical sites in Canada. Private sector contributions are facilitated by the Foundation for the National Institutes of Health (www.fnih.org). The grantee organization is the Northern California Institute for Research and Education, and the study is coordinated by the Alzheimer's Therapeutic Research Institute at the University of Southern California. ADNI data are disseminated by the Laboratory for Neuro Imaging at the University of Southern California.

ChatGPT (model GPT-4o) was used in January, March and July 2025 to assist with grammatics and to streamline parts of the text after initial drafting but we take full responsibility for the content of the manuscript.

References

1. 2024 Alzheimer's disease facts and figures. *Alzheimer's & Dementia: The Journal of the Alzheimer's Association* **20**(5), 3708–3821 (May 2024). <https://doi.org/10.1002/alz.13809>
2. Bach, S., Binder, A., Montavon, G., Klauschen, F., Müller, K.R., Samek, W.: On Pixel-Wise Explanations for Non-Linear Classifier Decisions by Layer-Wise Relevance Propagation. *PloS One* **10**(7), e0130140 (2015). <https://doi.org/10.1371/journal.pone.0130140>
3. Beach, T.G., Monsell, S.E., Phillips, L.E., Kukull, W.: Accuracy of the clinical diagnosis of Alzheimer disease at National Institute on Aging Alzheimer Disease Centers, 2005–2010. *Journal of Neuropathology and Experimental Neurology* **71**(4), 266–273 (Apr 2012). <https://doi.org/10.1097/NEN.0b013e31824b211b>
4. Bhagwat, N., Barry, A., Dickie, E.W., Brown, S.T., Devenyi, G.A., Hatano, K., DuPre, E., Dagher, A., Chakravarty, M., Greenwood, C.M.T., Misic, B., Kennedy, D.N., Poline, J.B.: Understanding the impact of preprocessing pipelines on neuroimaging cortical surface analyses. *GigaScience* **10**(1), giaa155 (Jan 2021). <https://doi.org/10.1093/gigascience/giaa155>
5. Böhle, M., Eitel, F., Weygandt, M., Ritter, K.: Layer-Wise Relevance Propagation for Explaining Deep Neural Network Decisions in MRI-Based Alzheimer's Disease Classification. *Frontiers in Aging Neuroscience* **11**, 194 (2019). <https://doi.org/10.3389/fnagi.2019.00194>
6. Bottani, S., Burgos, N., Maire, A., Saracino, D., Ströer, S., Dormont, D., Colliot, O., Alzheimer's Disease Neuroimaging Initiative, APPRIMAGE Study Group: Evaluation of MRI-based machine learning approaches for computer-aided diagnosis of dementia in a clinical data warehouse. *Medical Image Analysis* **89**, 102903 (Oct 2023). <https://doi.org/10.1016/j.media.2023.102903>
7. Bouthillier, X., Delaunay, P., Bronzi, M., Trofimov, A., Nichyporuk, B., Szeto, J., Mohammadi Sepahvand, N., Raff, E., Madan, K., Voleti, V., Ebrahimi Kahou, S., Michalski, V., Arbel, T., Pal, C., Varoquaux, G., Vincent, P.: Accounting for Variance in Machine Learning Benchmarks. In: Smola, A., Dimakis, A., Stoica, I. (eds.) *Proceedings of Machine Learning and Systems*. vol. 3, pp. 747–769 (2021), https://proceedings.mlsys.org/paper_files/paper/2021/file/0184b0cd3cfb185989f858a1d9f5c1eb-Paper.pdf
8. Bradshaw, T.J., Huemann, Z., Hu, J., Rahmim, A.: A Guide to Cross-Validation for Artificial Intelligence in Medical Imaging. *Radiology. Artificial Intelligence* **5**(4), e220232 (Jul 2023). <https://doi.org/10.1148/ryai.220232>
9. Canu, E., McLaren, D.G., Fitzgerald, M.E., Bendlin, B.B., Zoccatelli, G., Alessandrini, F., Pizzini, F.B., Ricciardi, G.K., Beltramello, A., Johnson, S.C., Frisoni, G.B.: Mapping the structural brain changes in Alzheimer's disease: The independent contribution of two imaging modalities. *Journal of Alzheimer's Disease* **26**(Suppl 3), 263–274 (2011). <https://doi.org/10.3233/JAD-2011-0040>, <https://www.ncbi.nlm.nih.gov/pmc/articles/PMC3267543/>
10. Damulina, A., Pirpamer, L., Soellradl, M., Sackl, M., Tinauer, C., Hofer, E., Enzinger, C., Gesierich, B., Duering, M., Ropele, S., Schmidt, R., Langkammer, C.: Cross-sectional and Longitudinal Assessment of Brain Iron Level in Alzheimer Disease Using 3-T MRI. *Radiology* **296**(3), 619–626 (Sep 2020). <https://doi.org/10.1148/radiol.2020192541>

11. Davatzikos, C.: Machine learning in neuroimaging: Progress and challenges. *NeuroImage* **197**, 652–656 (Aug 2019). <https://doi.org/10.1016/j.neuroimage.2018.10.003>
12. Dietterich, T.G.: Approximate Statistical Tests for Comparing Supervised Classification Learning Algorithms. *Neural Computation* **10**(7), 1895–1923 (Sep 1998). <https://doi.org/10.1162/089976698300017197>
13. Dinsdale, N.K., Bluemke, E., Smith, S.M., Arya, Z., Vidaurre, D., Jenkinson, M., Namburete, A.I.L.: Learning patterns of the ageing brain in MRI using deep convolutional networks. *NeuroImage* **224**, 117401 (Jan 2021). <https://doi.org/10.1016/j.neuroimage.2020.117401>
14. Dubois, B., Villain, N., Frisoni, G.B., Rabinovici, G.D., Sabbagh, M., Cappa, S., Bejanin, A., Bombois, S., Epelbaum, S., Teichmann, M., Habert, M.O., Nordberg, A., Blennow, K., Galasko, D., Stern, Y., Rowe, C.C., Salloway, S., Schneider, L.S., Cummings, J.L., Feldman, H.H.: Clinical diagnosis of Alzheimer's disease: recommendations of the International Working Group. *The Lancet. Neurology* **20**(6), 484–496 (Jun 2021). [https://doi.org/10.1016/S1474-4422\(21\)00066-1](https://doi.org/10.1016/S1474-4422(21)00066-1)
15. Eitel, F., Soehler, E., Bellmann-Strobl, J., Brandt, A.U., Ruprecht, K., Giess, R.M., Kuchling, J., Asseyer, S., Weygandt, M., Haynes, J.D., Scheel, M., Paul, F., Ritter, K.: Uncovering convolutional neural network decisions for diagnosing multiple sclerosis on conventional MRI using layer-wise relevance propagation. *NeuroImage. Clinical* **24**, 102003 (2019). <https://doi.org/10.1016/j.nicl.2019.102003>
16. Geirhos, R., Jacobsen, J.H., Michaelis, C., Zemel, R., Brendel, W., Bethge, M., Wichmann, F.A.: Shortcut learning in deep neural networks. *Nature Machine Intelligence* **2**(11), 665–673 (Nov 2020). <https://doi.org/10.1038/s42256-020-00257-z>, <https://www.nature.com/articles/s42256-020-00257-z>, publisher: Nature Publishing Group
17. Henneman, W.J.P., Sluimer, J.D., Barnes, J., van der Flier, W.M., Sluimer, I.C., Fox, N.C., Scheltens, P., Vrenken, H., Barkhof, F.: Hippocampal atrophy rates in Alzheimer disease: added value over whole brain volume measures. *Neurology* **72**(11), 999–1007 (Mar 2009). <https://doi.org/10.1212/01.wnl.0000344568.09360.31>
18. Hofmann, S.M., Beyer, F., Lapuschkin, S., Goltermann, O., Loeffler, M., Müller, K.R., Villringer, A., Samek, W., Witte, A.V.: Towards the interpretability of deep learning models for multi-modal neuroimaging: Finding structural changes of the ageing brain. *NeuroImage* **261**, 119504 (Nov 2022). <https://doi.org/10.1016/j.neuroimage.2022.119504>
19. Hofmann, S.M., Goltermann, O., Scherf, N., Müller, K.R., Löffler, M., Villringer, A., Gaebler, M., Witte, A.V., Beyer, F.: The utility of explainable AI for MRI analysis: Relating model predictions to neuroimaging features of the aging brain. *Imaging Neuroscience* **3**, imag_a_00497 (Feb 2025). https://doi.org/10.1162/imag_a_00497, https://doi.org/10.1162/imag_a_00497
20. Jenkinson, M., Beckmann, C.F., Behrens, T.E.J., Woolrich, M.W., Smith, S.M.: FSL. *NeuroImage* **62**(2), 782–790 (Aug 2012). <https://doi.org/10.1016/j.neuroimage.2011.09.015>
21. Kingma, D.P., Ba, J.: Adam: A Method for Stochastic Optimization. In: Bengio, Y., LeCun, Y. (eds.) 3rd International Conference on Learning Representations, ICLR 2015, San Diego, CA, USA, May 7-9, 2015, Conference Track Proceedings (2015), <http://arxiv.org/abs/1412.6980>
22. Kline, A., Luo, Y.: PsmPy: A Package for Retrospective Cohort Matching in Python. Annual International Conference of the IEEE Engineering in Medicine and Biology Society. IEEE Engineering in Medicine and Biology Society. Annual International Conference **2022**, 1354–1357 (Jul 2022). <https://doi.org/10.1109/EMBC48229.2022.9871333>
23. Kushol, R., Parnianpour, P., Wilman, A.H., Kalra, S., Yang, Y.H.: Effects of MRI scanner manufacturers in classification tasks with deep learning models. *Scientific Reports* **13**(1), 16791 (Oct 2023). <https://doi.org/10.1038/s41598-023-43715-5>
24. Lapuschkin, S., Wäldchen, S., Binder, A., Montavon, G., Samek, W., Müller, K.R.: Unmasking Clever Hans predictors and assessing what machines really learn. *Nature Communications* **10**(1), 1096 (Mar 2019). <https://doi.org/10.1038/s41467-019-08987-4>
25. Leonardsen, E.H., Persson, K., Grødem, E., Dinsdale, N., Schellhorn, T., Roe, J.M., Vidal-Piñeiro, D., Sørensen, Ø., Kaufmann, T., Westman, E., Marquand, A., Selbæk, G., Andreassen, O.A., Wolfers, T., Westlye, L.T., Wang, Y.: Constructing personalized characterizations of structural brain aberrations in

- patients with dementia using explainable artificial intelligence. *NPJ digital medicine* **7**(1), 110 (May 2024). <https://doi.org/10.1038/s41746-024-01123-7>
26. Lu, Y.C., Zuo, L., Chou, Y.Y., Dewey, B.E., Remedios, S., Shinohara, R.T., Steele, S.U., Nair, G., Reich, D.S., Prince, J.L., Pham, D.L.: An evaluation of image-based and statistical techniques for harmonizing brain volume measurements. *Imaging Neuroscience* **3**, IMAG.a.73 (Jul 2025). <https://doi.org/10.1162/IMAG.a.73>, <https://pmc.ncbi.nlm.nih.gov/articles/PMC12330838/>
 27. von Luxburg, U.: A tutorial on spectral clustering. *Statistics and Computing* **17**(4), 395–416 (Dec 2007). <https://doi.org/10.1007/s11222-007-9033-z>, <https://doi.org/10.1007/s11222-007-9033-z>
 28. Maaten, L.v.d., Hinton, G.: Visualizing Data using t-SNE. *Journal of Machine Learning Research* **9**(86), 2579–2605 (2008), <http://jmlr.org/papers/v9/vandermaaten08a.html>
 29. Malhi, B.S., Lo, J., Toto-Brocchi, M., Avval, A.H., Ma, Y., Du, J.: Quantitative magnetic resonance imaging in Alzheimer’s disease: a narrative review. *Quantitative Imaging in Medicine and Surgery* **15**(4), 3641–3664 (Apr 2025). <https://doi.org/10.21037/qims-24-1602>, <https://pmc.ncbi.nlm.nih.gov/articles/PMC11994541/>
 30. Marzi, C., Giannelli, M., Barucci, A., Tessa, C., Mascalchi, M., Diciotti, S.: Efficacy of MRI data harmonization in the age of machine learning: a multicenter study across 36 datasets. *Scientific Data* **11**(1), 115 (Jan 2024). <https://doi.org/10.1038/s41597-023-02421-7>
 31. Mattia, G.M., Villain, E., Nemmi, F., Le Lann, M.V., Franceris, X., Péran, P.: Investigating the discrimination ability of 3D convolutional neural networks applied to altered brain MRI parametric maps. *Artificial Intelligence in Medicine* **153**, 102897 (Jul 2024). <https://doi.org/10.1016/j.artmed.2024.102897>
 32. Montavon, G., Samek, W., Müller, K.R.: Methods for interpreting and understanding deep neural networks. *Digital Signal Processing* **73**, 1–15 (Feb 2018). <https://doi.org/10.1016/j.dsp.2017.10.011>, <https://www.sciencedirect.com/science/article/pii/S1051200417302385>
 33. Pfungst, O., Pfungst, O., Rahn, C.L.: Clever Hans (the horse of Mr. Von Osten) a contribution to experimental animal and human psychology. H. Holt and company, New York (1911). <https://doi.org/10.5962/bhl.title.56164>, <https://www.biodiversitylibrary.org/bibliography/56164>
 34. Scheltens, P., De Strooper, B., Kivipelto, M., Holstege, H., Chételat, G., Teunissen, C.E., Cummings, J., van der Flier, W.M.: Alzheimer’s disease. *The Lancet* **397**(10284), 1577–1590 (Apr 2021). [https://doi.org/10.1016/S0140-6736\(20\)32205-4](https://doi.org/10.1016/S0140-6736(20)32205-4), <https://www.sciencedirect.com/science/article/pii/S0140673620322054>
 35. Schmidt, R., Enzinger, C., Ropele, S., Schmidt, H., Fazekas, F., Austrian Stroke Prevention Study: Progression of cerebral white matter lesions: 6-year results of the Austrian Stroke Prevention Study. *Lancet* (London, England) **361**(9374), 2046–2048 (Jun 2003). [https://doi.org/10.1016/s0140-6736\(03\)13616-1](https://doi.org/10.1016/s0140-6736(03)13616-1)
 36. Serra, L., Cercignani, M., Lenzi, D., Perri, R., Fadda, L., Caltagirone, C., Macaluso, E., Bozzali, M.: Grey and white matter changes at different stages of Alzheimer’s disease. *Journal of Alzheimer’s disease: JAD* **19**(1), 147–159 (2010). <https://doi.org/10.3233/JAD-2010-1223>
 37. Simonyan, K., Vedaldi, A., Zisserman, A.: Deep Inside Convolutional Networks: Visualising Image Classification Models and Saliency Maps. In: Bengio, Y., LeCun, Y. (eds.) 2nd International Conference on Learning Representations, ICLR 2014, Banff, AB, Canada, April 14-16, 2014, Workshop Track Proceedings (2014), <http://arxiv.org/abs/1312.6034>
 38. Sluimer, J.D., Vrenken, H., Blankenstein, M.A., Fox, N.C., Scheltens, P., Barkhof, F., van der Flier, W.M.: Whole-brain atrophy rate in Alzheimer disease: identifying fast progressors. *Neurology* **70**(19 Pt 2), 1836–1841 (May 2008). <https://doi.org/10.1212/01.wnl.0000311446.61861.e3>
 39. Smith, S.M., Zhang, Y., Jenkinson, M., Chen, J., Matthews, P.M., Federico, A., De Stefano, N.: Accurate, robust, and automated longitudinal and cross-sectional brain change analysis. *NeuroImage* **17**(1), 479–489 (Sep 2002). <https://doi.org/10.1006/nimg.2002.1040>
 40. Springenberg, J.T., Dosovitskiy, A., Brox, T., Riedmiller, M.A.: Striving for Simplicity: The All Convolutional Net. In: Bengio, Y., LeCun, Y. (eds.) 3rd International Conference on Learning Representations, ICLR 2015, San Diego, CA, USA, May 7-9, 2015, Workshop Track Proceedings (2015), <http://arxiv.org/abs/1412.6806>

41. Tinauer, C., Damulina, A., Sackl, M., Soellradl, M., Achtibat, R., Dreyer, M., Pahde, F., Lapuschkin, S., Schmidt, R., Ropele, S., Samek, W., Langkammer, C.: Explainable Concept Mappings of MRI: Revealing the Mechanisms Underlying Deep Learning-Based Brain Disease Classification. In: Longo, L., Lapuschkin, S., Seifert, C. (eds.) Explainable Artificial Intelligence. pp. 202–216. Springer Nature Switzerland, Cham (2024). https://doi.org/10.1007/978-3-031-63797-1_11
42. Tinauer, C., Heber, S., Pirpamer, L., Damulina, A., Schmidt, R., Stollberger, R., Ropele, S., Langkammer, C.: Interpretable brain disease classification and relevance-guided deep learning. *Scientific Reports* **12**(1), 20254 (Nov 2022). <https://doi.org/10.1038/s41598-022-24541-7>
43. Tinauer, C., Sackl, M., Ropele, S., Langkammer, C.: Identifying Alzheimer's Disease Prediction Strategies of Convolutional Neural Network Classifiers using R2* Maps and Spectral Clustering. In: Proceedings 33rd European Signal Processing Conference EUSIPCO 2025. pp. 1497–1501 (2025), <https://eusipco2025.org/wp-content/uploads/pdfs/0001497.pdf>
44. Tustison, N.J., Avants, B.B., Cook, P.A., Zheng, Y., Egan, A., Yushkevich, P.A., Gee, J.C.: N4ITK: improved N3 bias correction. *IEEE transactions on medical imaging* **29**(6), 1310–1320 (Jun 2010). <https://doi.org/10.1109/TMI.2010.2046908>
45. Vásquez-Venegas, C., Wu, C., Sundar, S., Prôa, R., Bely, F.J., Medina, J.R., McNichol, M., Parvataneni, K., Kurtzman, N., Mirshawka, F., Aguirre-Jerez, M., Ebner, D.K., Celi, L.A.: Detecting and Mitigating the Clever Hans Effect in Medical Imaging: A Scoping Review. *Journal of Imaging Informatics in Medicine* (Nov 2024). <https://doi.org/10.1007/s10278-024-01335-z>
46. Wallis, D., Buvat, I.: Clever Hans effect found in a widely used brain tumour MRI dataset. *Medical Image Analysis* **77**, 102368 (Apr 2022). <https://doi.org/10.1016/j.media.2022.102368>
47. Wen, J., Thibreau-Sutre, E., Diaz-Melo, M., Samper-González, J., Routier, A., Bottani, S., Dormont, D., Durrleman, S., Burgos, N., Colliot, O., Alzheimer's Disease Neuroimaging Initiative, Australian Imaging Biomarkers and Lifestyle flagship study of ageing: Convolutional neural networks for classification of Alzheimer's disease: Overview and reproducible evaluation. *Medical Image Analysis* **63**, 101694 (Jul 2020). <https://doi.org/10.1016/j.media.2020.101694>
48. Westfall, P.H., Troendle, J.F., Pennello, G.: Multiple McNemar tests. *Biometrics* **66**(4), 1185–1191 (Dec 2010). <https://doi.org/10.1111/j.1541-0420.2010.01408.x>

Supplementary Material 1

Table 4 presents the distribution of preselected images across sites, vendors, and research groups, while Table 5 details their distribution across vendors, imaging protocols, and research groups.

Table 4: Distribution of preselected images by site, vendor and research group.

Phase	ADNI 2
Field Strength	3.0 tesla
Acquisition Plane	SAGITTAL
Pixel Spacing X	- multiple -
Pixel Spacing Y	- multiple -
Weighting	T1
Slice Thickness	1.2 mm

Count - Image Id	Research Group			
Site ID	Manufacturer	AD	CN	Total Result
002	Philips Medical Systems	8	84	92
003	GE MEDICAL SYSTEMS	36	78	114
005	GE MEDICAL SYSTEMS	31	3	34
006	Philips Medical Systems	34	52	86
007	GE MEDICAL SYSTEMS	22	60	82
009	SIEMENS	23	44	67
010	Philips Medical Systems	2	20	22
011	SIEMENS	36	75	111
012	Philips Medical Systems		36	36
013	Philips Medical Systems	6	26	32
	SIEMENS	4	12	16
014	SIEMENS	18	46	64
016	GE MEDICAL SYSTEMS	50	52	102
	SIEMENS		2	2
018	Philips Medical Systems	18	54	72
019	Philips Medical Systems	45	24	69
021	GE MEDICAL SYSTEMS	10	55	65
022	SIEMENS		56	56
023	SIEMENS	16	38	54
024	SIEMENS	34	24	58
027	GE MEDICAL SYSTEMS	40		40
029	GE MEDICAL SYSTEMS	8	69	77
031	Philips Medical Systems	8	48	56
032	SIEMENS	8	48	56
033	SIEMENS	24	56	80
035	SIEMENS	6	29	35
036	SIEMENS	34	32	66
	SIEMENS PixelMed	2	2	4
037	SIEMENS	31	65	96
041	SIEMENS		80	80
051	SIEMENS	15		15
052	GE MEDICAL SYSTEMS	16		16
053	Philips Medical Systems	10	12	22
057	GE MEDICAL SYSTEMS		4	4
	SIEMENS	2		2
067	SIEMENS	12	12	24
068	SIEMENS	10	28	38
070	SIEMENS	6	20	26

072	SIEMENS	18	18
073	SIEMENS	11	122
082	SIEMENS	9	48
094	GE MEDICAL SYSTEMS	21	52
098	GE MEDICAL SYSTEMS	16	56
099	GE MEDICAL SYSTEMS		12
	SIEMENS	6	24
100	Philips Medical Systems	2	24
109	GE MEDICAL SYSTEMS	2	10
114	SIEMENS	9	5
116	SIEMENS	43	70
123	SIEMENS	10	2
126	GE MEDICAL SYSTEMS	18	18
127	GE MEDICAL SYSTEMS	69	58
128	SIEMENS	20	52
129	GE MEDICAL SYSTEMS		38
	Philips Healthcare	16	16
130	Philips Medical Systems	83	24
131	GE MEDICAL SYSTEMS		8
	Philips Healthcare	4	4
135	SIEMENS	44	34
136	Philips Medical Systems	2	20
137	SIEMENS	38	72
141	SIEMENS		2
153	SIEMENS	10	38
941	SIEMENS		76
Total Result		1042	2227
			3269

Table 5: Distribution of preselected images by vendor, imaging protocol and research group.

Phase	ADNI 2
Acquisition Plane	SAGITTAL
Field Strength	3.0 tesla
Pixel Spacing X	- multiple -
Pixel Spacing Y	- multiple -
Weighting	T1
Slice Thickness	1.2 mm

Count - Image Id		Research Group		
Manufacturer	Description	AD	CN	Total Result
GE MEDICAL SYSTEMS	Accelerated Sag IR-FSPGR	59	55	114
	Accelerated Sag IR-SPGR	105	191	296
	Accelerated SAG IR-SPGR REPEAT		2	2
	IR-SPGR	3	28	31
	IR-SPGR w/acceleration	3	28	31
	Sag IR-FSPGR	59	57	116
	Sag IR-SPGR	109	194	303
	Sag IR-SPGR REPEAT	1		1
Philips Healthcare	MPRAGE	2	8	10
	MPRAGE SENSE2	2	8	10
Philips Medical Systems	MPRAGE	108	212	320
	MPRAGE SENSE		1	1
	MPRAGE SENSE2	110	210	320
	MPRAGE SENSE2 SENSE		1	1
SIEMENS	MPRAGE	233	579	812
	MPRAGE GRAPPA 2	1	3	4
	MPRAGE GRAPPA 2_ND	1	3	4
	MPRAGE GRAPPA2	181	487	668
	MPRAGE GRAPPA2_S3_DIS3D		2	2
	MPRAGE Repeat	1		1
	MPRAGE_NO ANGLE		2	2
	MPRAGE_NO ANGLE=		12	12
	MPRAGE_Sag - NO ANGLE=	2	3	5
	MPRAGE_GRAPPA2	48	84	132
	MPRAGE_ND	1	3	4
	MPRAGE_P2_NO ANGLE		2	2
	MPRAGE_P2_NO ANGLE=	2	15	17
	MPRAGE_S2_DIS2D		1	1
	MPRAGE_S2_DIS3D	1	16	17
SIEMENS PixelMed	SAG MPRAGE GRAPPA2 NO ANGLE	4	9	13
	SAG MPRAGE NO ANGLE	4	9	13
Total Result		1042	2227	3269

Figure 4 shows standardized mean differences across covariates before and after propensity-logit-matching. APOE $\epsilon 4$ carrier status, which has been associated with subtle regional gray matter and hippocampal volume differences even in cognitively normal individuals, was not included as a matching covariate. As the objective of this study was to assess preprocessing- and model-related biases rather than genetic or disease-risk effects, only age and sex were used for propensity matching. The resulting variation in APOE $\epsilon 4$ distribution was therefore considered to reflect natural biological heterogeneity between groups and is therefore reflected in the effect size.

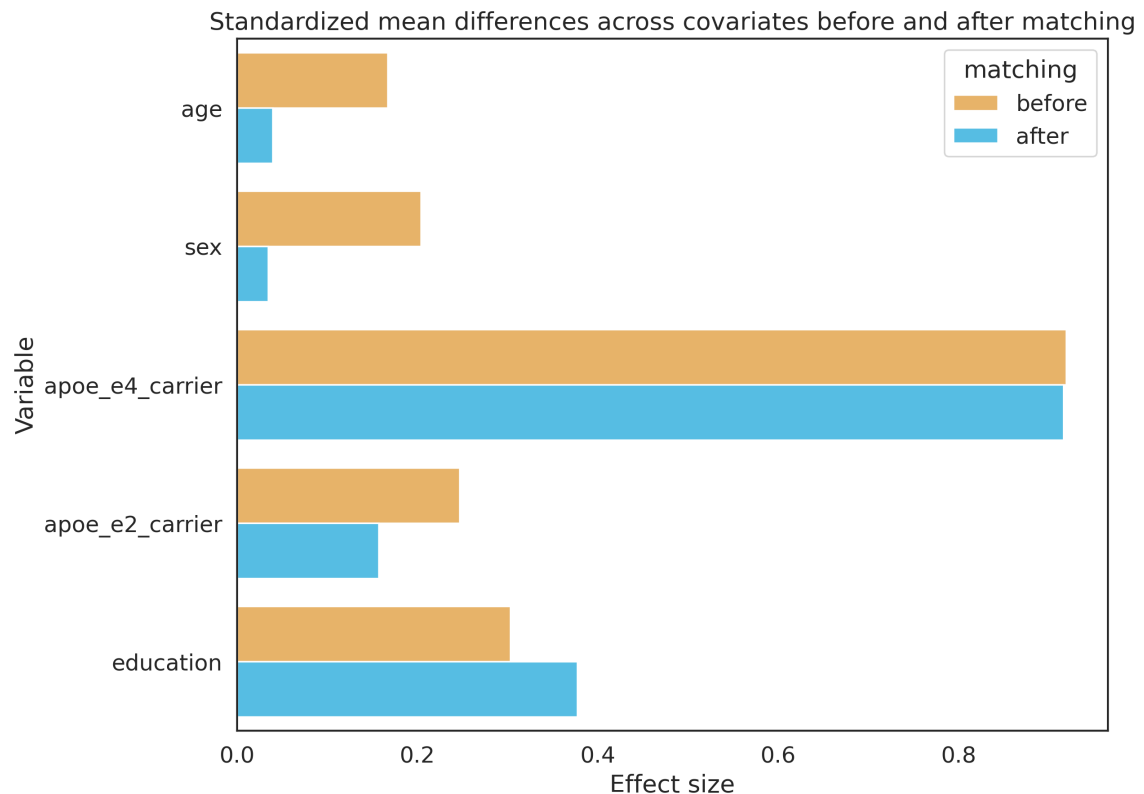


Fig. 4: Standardized mean differences across covariates before and after matching. Only variables age and sex were used for propensity-logit-matching.

Although the binarization thresholds in the model setup were chosen arbitrarily, Figure 5 illustrates that they were selected to preserve meaningful atrophy patterns by comparing residual voxels with individual brain masks. Thresholds above 50% were excluded, as they resulted in visually unrealistic images not identifiable as brains.

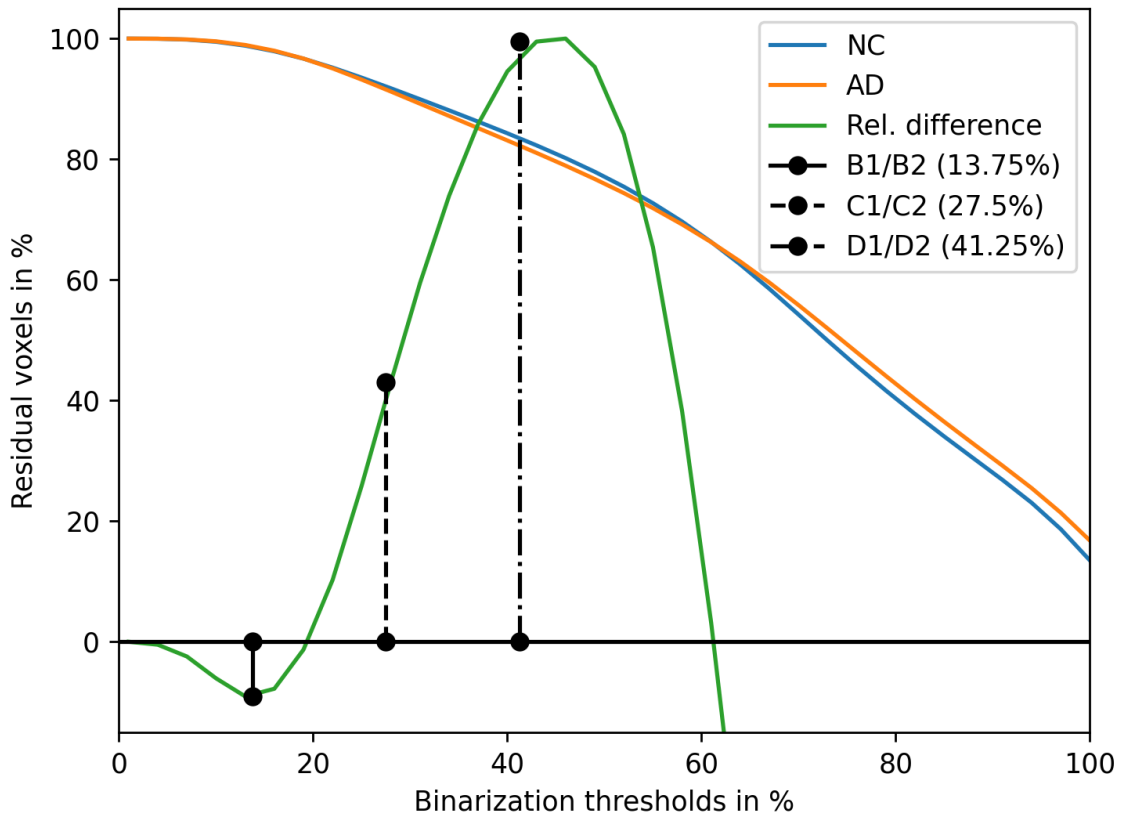


Fig. 5: Residual voxels expressed as a percentage of the brain mask across binarization thresholds. Normalized group differences (NC vs. AD) are shown, with black lines indicating thresholds applied in the model setups.

Supplementary Material 2

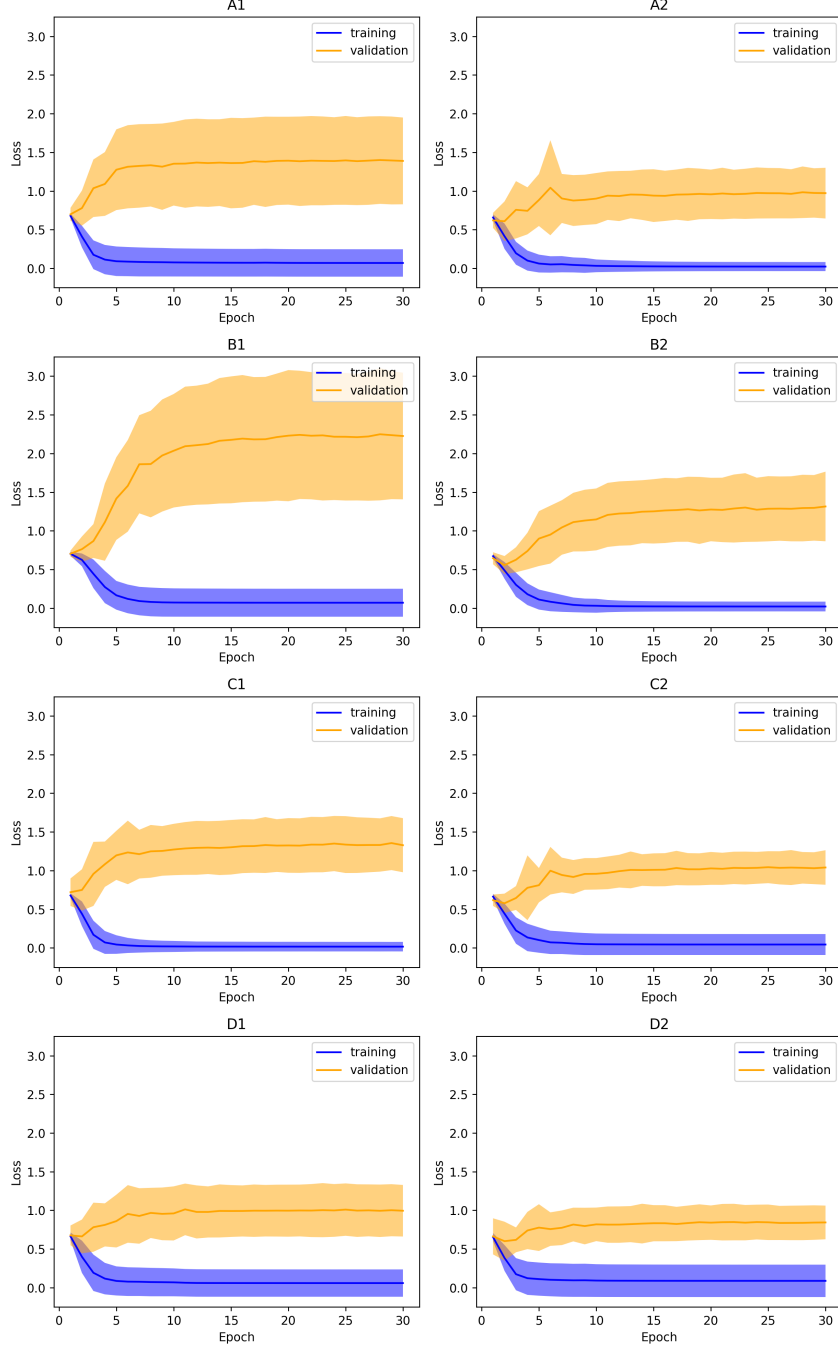


Fig. 6: Mean and standard deviation of training (blue) and validation (orange) loss curves over epochs for all setups. Training loss decreases smoothly, while validation loss slightly rises before stabilizing. Both curves plateau after 10 epochs, indicating convergence. The gap between training and validation losses suggests minimal overfitting. The model architecture was optimized for setup A2.

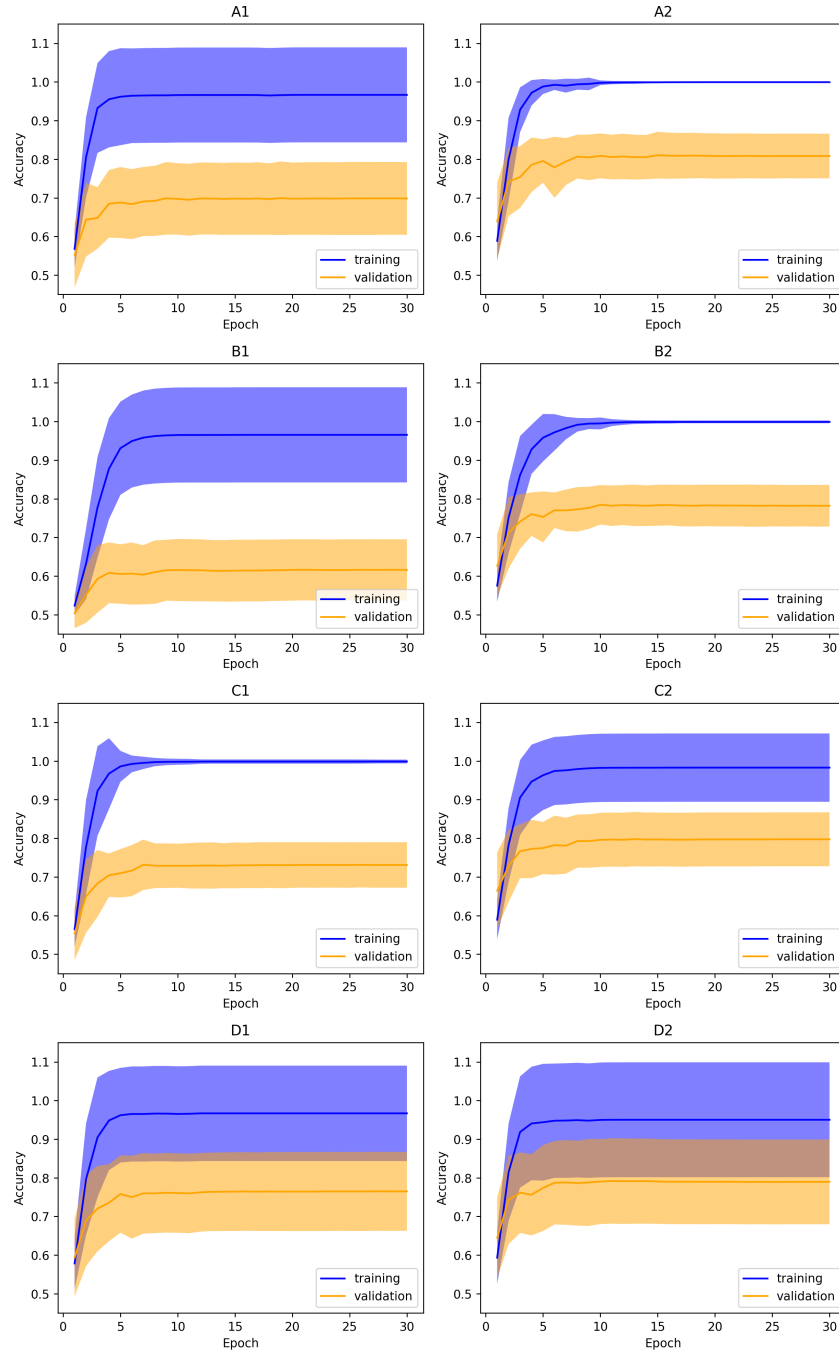


Fig. 7: Mean and standard deviation of training (blue) and validation (orange) accuracy curves over epochs for all setups.

Supplementary Material 3

Table 6: Multiple testing using two-sided p-values for multiple models and performance measures. Note. Comparison denotes models and measure; e.g., “A2-B1, acc” compares models A2 (skull-stripped, no-binarization) and B1 (binarized-13.75%) with respect to the overall accuracy. Θ_1 and Θ_2 refers to the respective performance metrics. Adj. p-value is the discrete Bonferroni-Holm corrected p-value of the comparison. The table shows only the 122 significant differences of the multiple testing and the first non-significant difference. Remaining results are indicated with “(477 more)”.

Comparison	Θ_1	Θ_2	Sampling Index	Initial Weights Index	Adj. p-value
A2-B1, acc	0.84	0.55	9	2	0.00000
A2-B1, acc	0.89	0.58	9	3	0.00000
A2-B1, acc	0.88	0.61	2	3	0.00000
A2-B1, acc	0.83	0.54	8	1	0.00000
A2-B1, spe	0.89	0.50	9	2	0.00000
A2-C1, spe	0.89	0.52	9	2	0.00000
A2-B1, acc	0.84	0.62	7	3	0.00000
A2-B1, acc	0.80	0.53	4	1	0.00000
A2-A1, acc	0.86	0.68	1	2	0.00000
A2-B1, spe	0.94	0.64	7	3	0.00000
A2-B1, acc	0.83	0.58	2	2	0.00000
A2-B1, acc	0.87	0.62	10	2	0.00000
A2-B1, acc	0.84	0.59	9	1	0.00000
A2-B1, acc	0.86	0.63	4	2	0.00000
A2-A1, sen	0.90	0.57	10	2	0.00000
A2-B1, sen	0.93	0.63	9	3	0.00000
A2-A1, sen	0.87	0.60	1	2	0.00000
A2-A1, spe	0.94	0.69	7	3	0.00000
A2-C1, acc	0.84	0.61	9	2	0.00000
A2-B1, sen	0.90	0.59	3	3	0.00000
A2-C1, spe	0.82	0.52	1	3	0.00000
A2-B1, acc	0.86	0.68	1	2	0.00000
A2-C1, acc	0.86	0.67	1	2	0.00000
A2-A1, acc	0.82	0.60	4	3	0.00000
A2-B1, acc	0.79	0.57	5	3	0.00000
A2-B1, spe	0.89	0.61	9	1	0.00000
A2-B1, acc	0.81	0.61	10	1	0.00000
A2-B1, sen	0.87	0.58	10	3	0.00000
A2-B1, sen	0.80	0.47	8	1	0.00000
A2-B1, sen	0.82	0.51	2	3	0.00000
A2-B1, sen	0.90	0.60	10	2	0.00001
A2-A1, acc	0.86	0.67	4	2	0.00001
A2-B2, acc	0.89	0.73	9	3	0.00001
A2-B1, acc	0.81	0.59	8	2	0.00001

A2-B1, spe	0.85	0.52	9	3	0.00001
A2-C1, acc	0.83	0.64	8	1	0.00001
A2-A1, acc	0.87	0.70	10	2	0.00001
A2-B1, spe	0.94	0.72	2	3	0.00001
A2-B1, spe	0.90	0.62	4	2	0.00001
A2-B1, acc	0.81	0.63	3	1	0.00002
A2-C1, acc	0.81	0.61	8	2	0.00002
A2-B1, acc	0.76	0.56	10	3	0.00003
A2-D2, spe	0.85	0.66	10	2	0.00003
A2-B1, spe	0.87	0.61	4	3	0.00004
A2-C1, sen	0.90	0.64	10	2	0.00004
A2-B2, spe	0.66	0.89	10	3	0.00006
A2-D1, sen	0.82	0.53	4	2	0.00006
A2-A1, acc	0.81	0.62	8	2	0.00007
A2-C1, sen	0.80	0.55	8	1	0.00008
A2-C1, acc	0.87	0.71	10	2	0.00008
A2-B1, acc	0.82	0.64	4	3	0.00008
A2-D1, acc	0.86	0.71	1	2	0.00009
A2-B1, spe	0.83	0.52	4	1	0.00009
A2-A1, spe	0.90	0.64	4	2	0.00011
A2-A1, sen	0.94	0.74	5	2	0.00013
A2-B1, spe	0.86	0.61	8	1	0.00014
A2-B1, acc	0.84	0.68	1	1	0.00015
A2-B1, sen	0.81	0.54	2	2	0.00024
A2-A1, acc	0.88	0.75	2	3	0.00025
A2-A1, sen	0.75	0.47	8	2	0.00025
A2-A1, acc	0.81	0.66	3	1	0.00028
A2-C1, acc	0.81	0.66	1	3	0.00031
A2-D1, spe	0.66	0.87	10	3	0.00032
A2-C1, sen	0.87	0.64	1	2	0.00034
A2-B1, sen	0.78	0.54	4	1	0.00039
A2-A1, spe	0.87	0.66	4	3	0.00042
A2-B1, acc	0.82	0.67	7	2	0.00052
A2-B1, spe	0.85	0.62	2	2	0.00065
A2-B1, spe	0.92	0.71	7	1	0.00105
A2-D1, sen	0.90	0.66	10	2	0.00104
A2-B1, spe	0.83	0.60	3	1	0.00108
A2-C1, acc	0.82	0.69	7	2	0.00162
A2-C1, acc	0.89	0.75	9	3	0.00161
A2-B2, sen	0.82	0.63	4	2	0.00224
A2-D2, acc	0.79	0.89	5	3	0.00224
A2-B1, sen	0.75	0.48	8	2	0.00235
A2-D2, sen	0.78	0.58	4	1	0.00278
A2-B2, acc	0.86	0.74	4	2	0.00281

A2-B1, acc	0.80	0.66	7	1	0.00285
A2-B2, spe	0.85	0.64	9	3	0.00289
A2-D2, spe	0.65	0.81	5	3	0.00294
A2-A1, spe	0.89	0.71	9	2	0.00385
A2-A1, acc	0.84	0.72	1	1	0.00471
A2-D1, acc	0.86	0.71	4	2	0.00612
A2-B1, spe	0.80	0.59	10	1	0.00760
A2-D1, sen	0.87	0.66	1	2	0.00759
A2-B1, sen	0.82	0.60	6	1	0.00776
A2-B2, spe	0.94	0.76	7	3	0.00774
A2-C1, spe	0.88	0.65	8	2	0.00779
A2-A1, sen	0.81	0.62	2	1	0.00786
A2-A1, acc	0.82	0.69	7	2	0.00822
A2-B1, spe	0.65	0.39	5	3	0.00861
A2-A1, acc	0.89	0.77	9	3	0.00975
A2-B2, sen	0.75	0.88	7	3	0.00985
A2-B1, sen	0.79	0.59	9	2	0.01137
A2-C1, sen	0.81	0.61	2	2	0.01135
A2-A1, sen	0.79	0.59	1	3	0.01203
A2-B1, spe	0.85	0.67	1	2	0.01280
A2-A1, acc	0.80	0.69	7	1	0.01469
A2-B1, spe	0.85	0.63	10	2	0.01656
A2-A1, acc	0.79	0.68	2	1	0.01664
A2-A1, spe	0.94	0.79	2	3	0.01694
A2-D1, spe	0.65	0.85	5	3	0.01915
A2-C1, sen	0.93	0.77	9	3	0.01916
A2-C1, acc	0.81	0.68	10	1	0.01927
A2-A1, spe	0.90	0.72	7	2	0.02008
A2-C1, sen	0.90	0.73	3	3	0.02038
A2-B1, sen	0.87	0.69	1	2	0.02084
A2-C1, acc	0.83	0.70	2	2	0.02126
A2-B1, sen	0.79	0.57	9	1	0.02497
A2-B1, spe	0.88	0.69	1	1	0.02553
A2-C1, acc	0.86	0.72	4	2	0.02597
A2-A1, acc	0.83	0.71	8	1	0.02820
A2-B2, spe	0.66	0.81	3	3	0.02896
A2-B1, spe	0.90	0.72	7	2	0.02998
A2-C2, spe	0.66	0.81	3	3	0.03210
A2-A1, sen	0.82	0.64	10	1	0.03369
A2-B1, sen	0.93	0.75	5	3	0.03393
A2-A1, acc	0.84	0.74	7	3	0.03642
A2-B1, acc	0.77	0.63	3	2	0.03756
A2-B1, acc	0.79	0.66	2	1	0.03768
A2-C1, acc	0.81	0.69	3	1	0.03935

A2-C1, spe	0.89	0.72	9	1	0.05069
(477 more)	:	:	:	:	:

Supplementary Material 4

Table 7 presents the demographic characteristics of our local, non-public datasets at baseline. These datasets were age-matched to the subset of ADNI data used for model training. The corresponding model performance on these local datasets is summarized in Table 8.

The reference model (A2) exhibits an average performance decline of approximately 9% compared to its test performance on ADNI data. Models B2 and C2 perform near chance level, while model D2 shows a performance drop of about 13%. Notably, model A1 achieves nearly identical average performance on both the ADNI test set and our local datasets. Although models B1 and C1 underperform on the local data, the decline observed for model D1 is more moderate (approximately 8%).

Importantly, the image preprocessing steps were identical for both ADNI and local datasets. To investigate potential causes of the performance discrepancies, we examined volume distributions across cohorts (Figure 8). When skull-stripping was applied, a systematic offset was observed between the ADNI data and our local datasets. This offset may account for the pronounced performance decline in models B2 and C2, which rely primarily on volumetric features, as well as in model D2, which retains more structural information. The observed volume shift also suggests a potential contribution of skull-stripping to the diminished performance of model A2.

Table 7: Summary of subject demographics at baseline for our local, non-public datasets. Note. Values are presented as mean \pm SD [range]. M: male, F: female, MMSE: mini-mental state examination, CDR: global clinical dementia rating, APOE: Apolipoprotein E status, Education in years, ASPS = Austrian Stroke Prevention Study [35] used as group normal control, ProDem = Prospective Dementia Registry Austria [10] used as group Alzheimer's disease, n/a: no value available. *CDR scores for ASPS were acquired at followup, no baseline is available.

	Subjects	Images	Age	Gender	MMSE	CDR	APOE	Education
ASPS	304	401	71.2 \pm 6.3 [55.7, 87.2]	119 M/ 185 F	27.9 \pm 1.6 [22.0, 30.0] n/a: 0	0.5: 21; n/a: 283*	ϵ_2/ϵ_2 : 2; ϵ_2/ϵ_3 : 33; ϵ_2/ϵ_4 : 1; ϵ_3/ϵ_3 : 209; ϵ_3/ϵ_4 : 43; ϵ_4/ϵ_4 : 4; n/a: 12	11.3 \pm 2.8 [9.0, 18.0] n/a: 0
ProDem	178	358	73.3 \pm 8.0 [55.7, 90.7]	75 M/ 103 F	21.7 \pm 4.2 [7.0, 29.0] n/a: 1	0.5: 90; 1.0: 77; 2.0: 6; n/a: 5	ϵ_2/ϵ_2 : 1; ϵ_2/ϵ_3 : 7; ϵ_2/ϵ_4 : 7; ϵ_3/ϵ_3 : 87; ϵ_3/ϵ_4 : 67; ϵ_4/ϵ_4 : 8; n/a: 1	11.0 \pm 2.7 [9.0, 18.0] n/a: 1

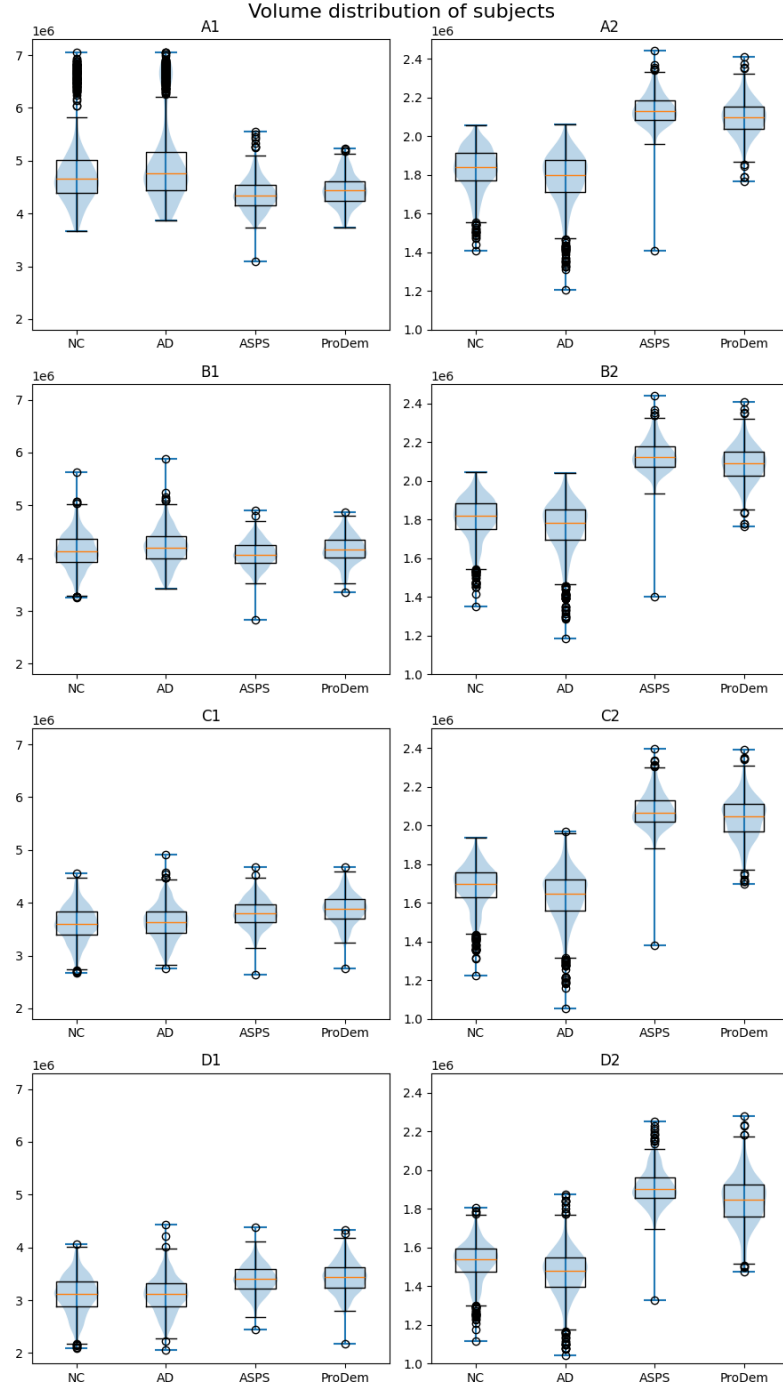


Fig. 8: Comparison of total voxel count distributions between NC and AD groups from ADNI and our local cohorts ASPS (as controls) and ProDem (as patients) across the eight image setups. The left column shows (A1) aligned T1w MRIs and corresponding binarized images using thresholds of (B1) 13.75%, (C1) 27.50%, and (D1) 41.25%. The right column displays the skull-stripped versions (A2, B2, C2, D2). Distributions are similar in the left column, while skull-stripping introduces a group-dependent offset in voxel counts. For A1 and A2, a low binarization threshold (5% of white matter peak) was used to suppress background voxels.

Table 8: Summary of performance metrics of all configurations on local datasets (ASPS [35], Pro-Dem [10]). Note. AUC = area under receiver operating characteristics curve. Column Id refers to preprocessing defined in Figure 1. Values between [and] show the 95% confidence interval.

Input images	Id	Binarizer	Accuracy	Sensitivity	Specificity	AUC
Aligned T1w	A1	None	72.31 \pm 2.11% [68.87%, 75.75%]	58.75 \pm 7.16% [47.32%, 71.97%]	84.41 \pm 5.15% [75.65%, 93.27%]	0.72 \pm 0.022 [0.68, 0.75]
	B1	13.75%	52.53 \pm 3.22% [47.52%, 58.54%]	61.27 \pm 14.33% [35.22%, 84.89%]	44.72 \pm 16.19% [18.79%, 71.02%]	0.53 \pm 0.028 [0.49, 0.58]
	C1	27.50%	51.93 \pm 3.91% [46.25%, 59.30%]	70.25 \pm 16.62% [38.67%, 93.88%]	35.58 \pm 20.35% [4.49%, 69.94%]	0.53 \pm 0.032 [0.48, 0.59]
	D1	41.25%	69.50 \pm 3.43% [61.95%, 74.59%]	63.77 \pm 10.27% [46.96%, 84.39%]	74.63 \pm 11.62% [51.06%, 91.17%]	0.69 \pm 0.033 [0.62, 0.74]
Skull-stripped T1w	A2	None	72.90\pm4.37% [63.21%, 79.78%]	70.66\pm11.78% [50.89%, 91.09%]	74.90 \pm 16.19% [39.84%, 94.51%]	0.73\pm0.039 [0.64, 0.79]
	B2	13.75%	58.47 \pm 5.55% [47.93%, 68.32%]	54.72 \pm 17.37% [24.88%, 80.33%]	61.81 \pm 23.95% [22.17%, 93.90%]	0.58 \pm 0.047 [0.49, 0.67]
	C2	27.50%	52.20 \pm 5.63% [44.60%, 63.69%]	69.76 \pm 16.61% [33.91%, 96.01%]	36.51 \pm 23.81% [0.42%, 82.17%]	0.53 \pm 0.047 [0.46, 0.62]
	D2	41.25%	68.11 \pm 5.33% [57.33%, 75.11%]	62.96 \pm 13.70% [36.56%, 84.71%]	72.71 \pm 17.65% [38.24%, 95.40%]	0.68 \pm 0.049 [0.58, 0.75]

Supplementary Material 5

Introduction to spectral relevance analysis

Spectral relevance analysis (SpRAy) enables efficient exploration of classifier behavior across large datasets by applying spectral clustering to inputs and heatmaps. This technique identifies common and atypical decision-making patterns, highlighting image features that may or may not reflect clinically relevant concepts. SpRAy is useful for uncovering unexpected or artifact-driven classifier behaviors, similar to the Clever Hans effect found in [24].

The SpRAy process implemented for this study involves five steps:

1. Compute relevance maps using LRP to identify focus areas for classification.
2. Downsample the inputs and the heatmaps to 2 mm isotropic resolution for efficient analysis.
3. Perform spectral clustering to group similar image or relevance patterns.
4. Identify clusters with highest eigenvalue gap, indicating well-separated groups, and compute mean heatmaps for groups.

Visualize the clusters using t-distributed stochastic neighbor embedding (t-SNE) [28], which aids in interpreting the results and understanding the relationship between clusters.

Results of spectral relevance analysis

We visualized the clustering of inputs and heatmaps using t-SNE, initialized with the normalized, symmetric, and positive semi-definite Laplacian matrix derived from the spectral clustering affinity matrix. Figure 9 illustrates the grouping of inputs and corresponding heatmaps for the reference model (skull-stripped, no binarization, A2), the 27.5% binarized skull-stripped model (C2), and the 41.25% binarized model without skull-stripping (D1). Group mean heatmaps, based on spectral clustering groupings, are presented in Figure 10.

The analysis of the eigenvalues and the eigenvalue gaps of the Laplacians and the t-SNE visualization of input and heatmap groupings for all eight models are given in Figures 11, 12, 13, and 14. Additionally, Figures 15 and 16 present the analysis of misclassified samples and the corresponding heatmaps for models A2 and C2 using SpRAy.

Discussion of spectral relevance analysis

The t-SNE visualization of input images and corresponding heatmaps in Figure 9 demonstrated that only the 41.25% binarized model without skull-stripping (D1) exhibited a heatmap grouping aligned with the underlying subject groups (NC vs. AD) while having similar classification performance as the reference model (A2). This suggests that models trained on highly preprocessed images, such as skull-stripped or lower-threshold binarized data, may introduce additional biases that alter feature utilization. The observed eigenvalue gaps (see Figures 11, 12, 13, and 14) further confirmed the presence of distinct classifier behaviors, with spectral clustering successfully distinguishing dominant and atypical relevance patterns.

The mean heatmaps in Figure 10, derived from heatmap spectral clustering groupings, highlight

consistent relevance patterns, offering insight into the classifier's decision strategies. In model D1 (41.25% binarization without skull-stripping), the separation between AD (Group 2) and NC (Group 1) predictions is more pronounced than in models A2 (reference) and C2 (27.5% binarization with skull-stripping). The Group 2 mean heatmap in model D1 shows distinct relevance in the left insular cortex, suggesting a more structured and positionally distinct relevance pattern, consistent with the clustering observed in the t-SNE visualization. Group 3, while similar to Group 2, also highlights regions in the skull, which is an unexpected decision strategy for classifying AD.

Similar patterns are found for the misclassification analysis in Figures 15 and 16.

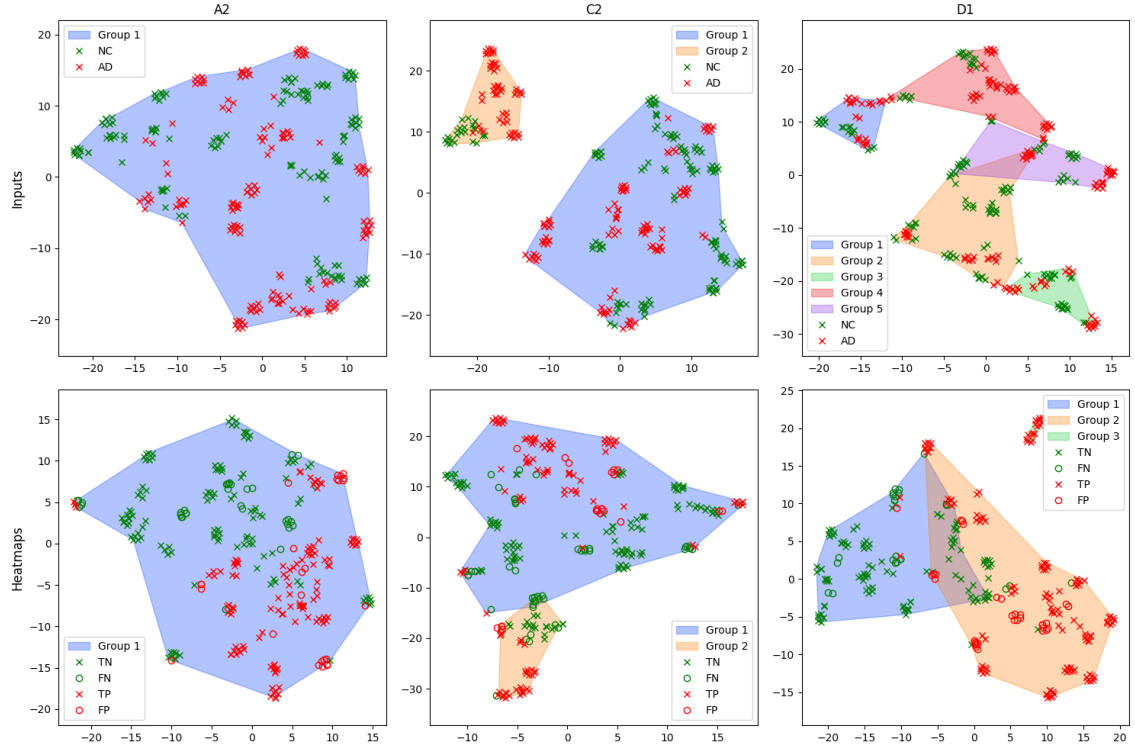


Fig. 9: t-SNE visualization of inputs (row 1) and heatmaps (row 2) for the reference model (A2), the 27.5% binarization model (C2), and the 41.25% binarization model without skull-stripping (D1). Input data points are labeled by group (NC or AD), while heatmap points are categorized by confusion matrix outcomes (TN, FN, TP, FP). Only the heatmaps of model D1 exhibit clustering that aligns with the subject groups (NC vs. AD). Note. NC: normal control; AD: Alzheimer's disease; TN: true negative; FN: false negative; TP: true positive; FP: false positive.

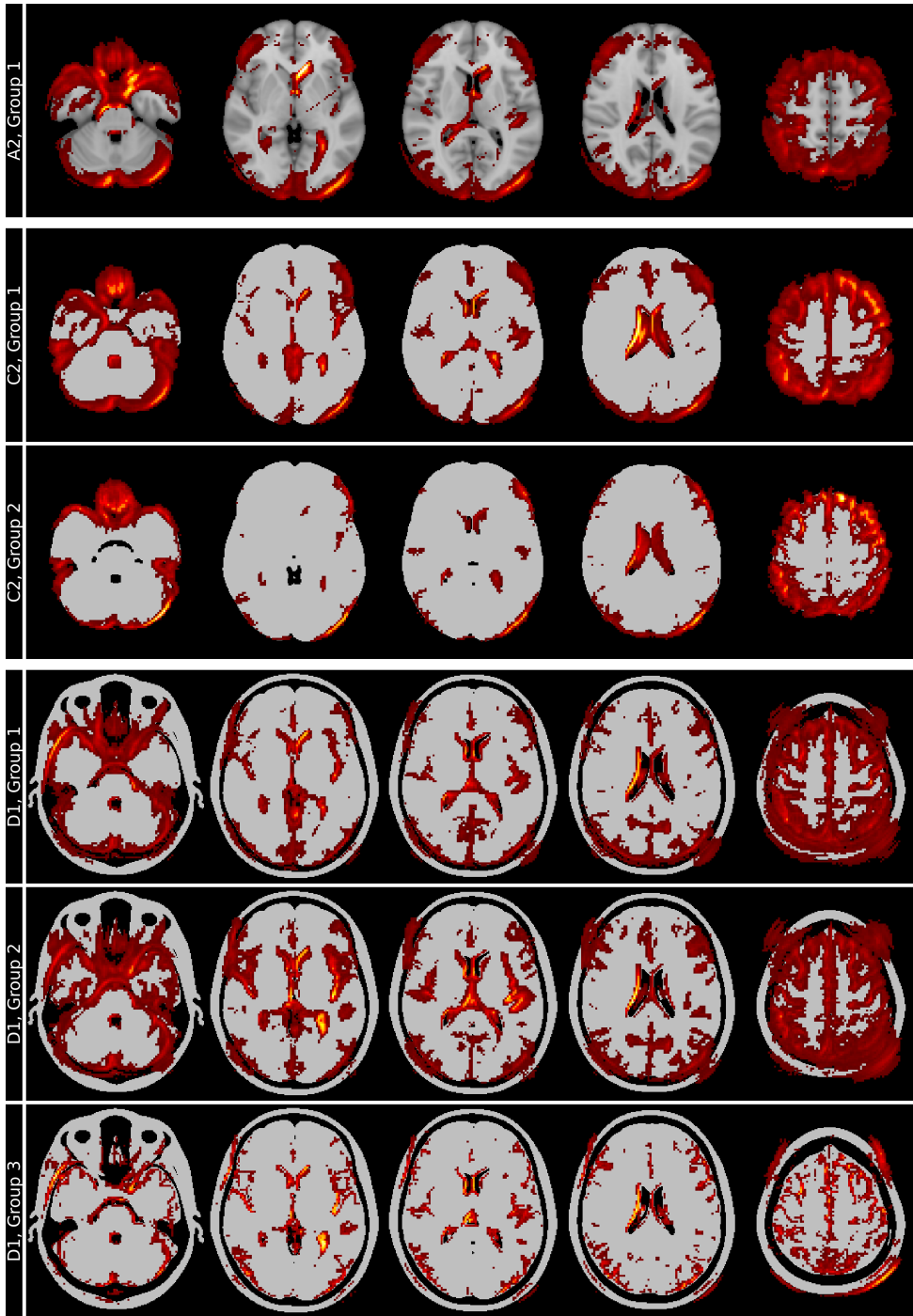


Fig. 10: Mean heatmaps for the groups identified using the individual heatmaps and spectral clustering for models A2, C2, and D1. Model D1 (41.25% binarization without skull-stripping) shows a clearer separation between AD (Group 2) and NC (Group 1) than A2 and C2. Group 2 in D1 highlights the left insular cortex, suggesting a more structured relevance pattern. Group 3, similar to Group 2, also shows relevance in the skull, indicating an unexpected decision strategy for AD classification. Images are shown in standard-radiological view, causing the left and right side of the brain to be flipped.

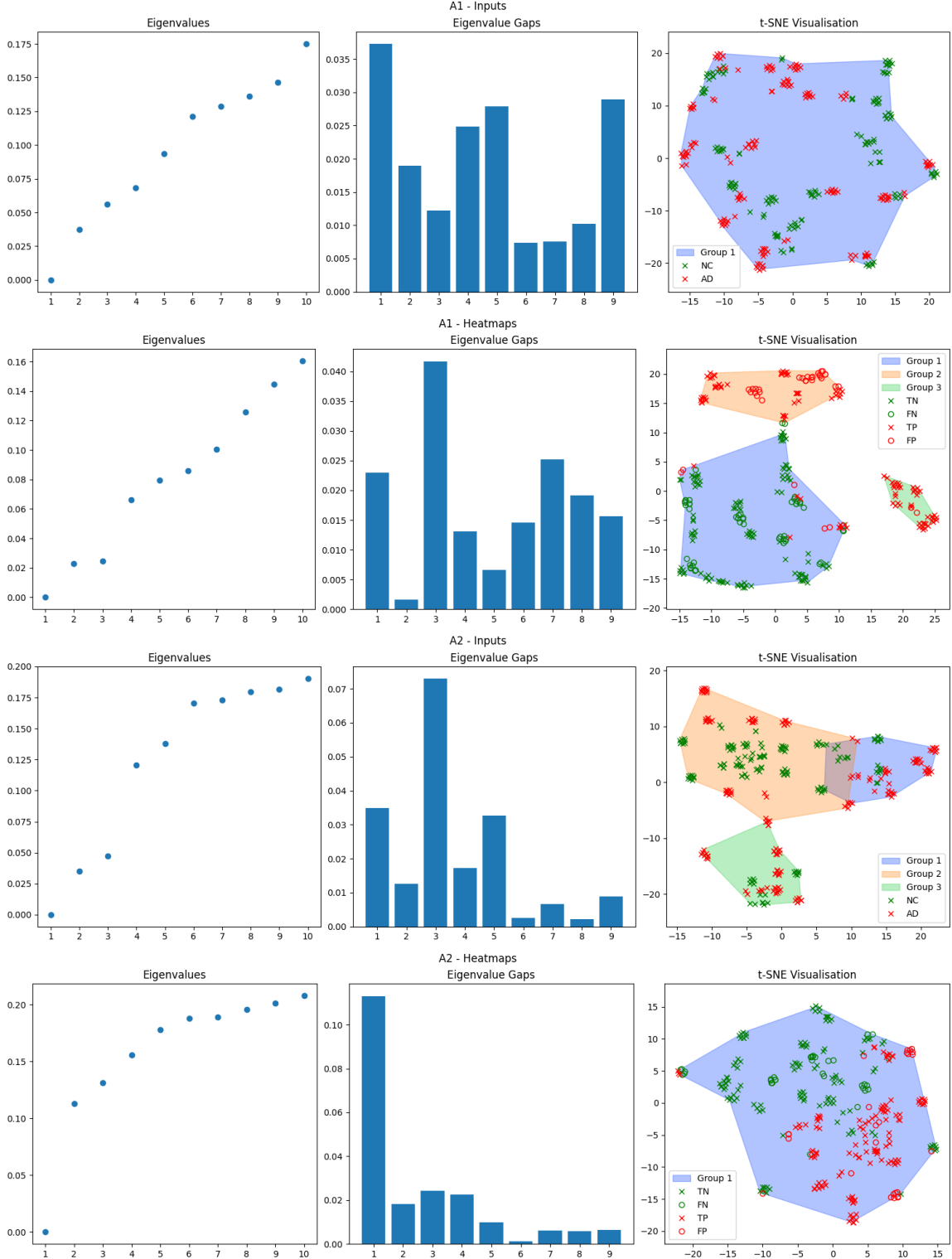


Fig. 11: Eigenvalues (column 1), the respective eigenvalue gaps (column 2) of the Laplacian matrix and the and t-SNE visualization (column 3) of input (rows 1 and 3) and heatmap groupings (rows 2 and 4) for models A1 (aligned T1w MRI) and A2 (skull-stripped T1w MRI).

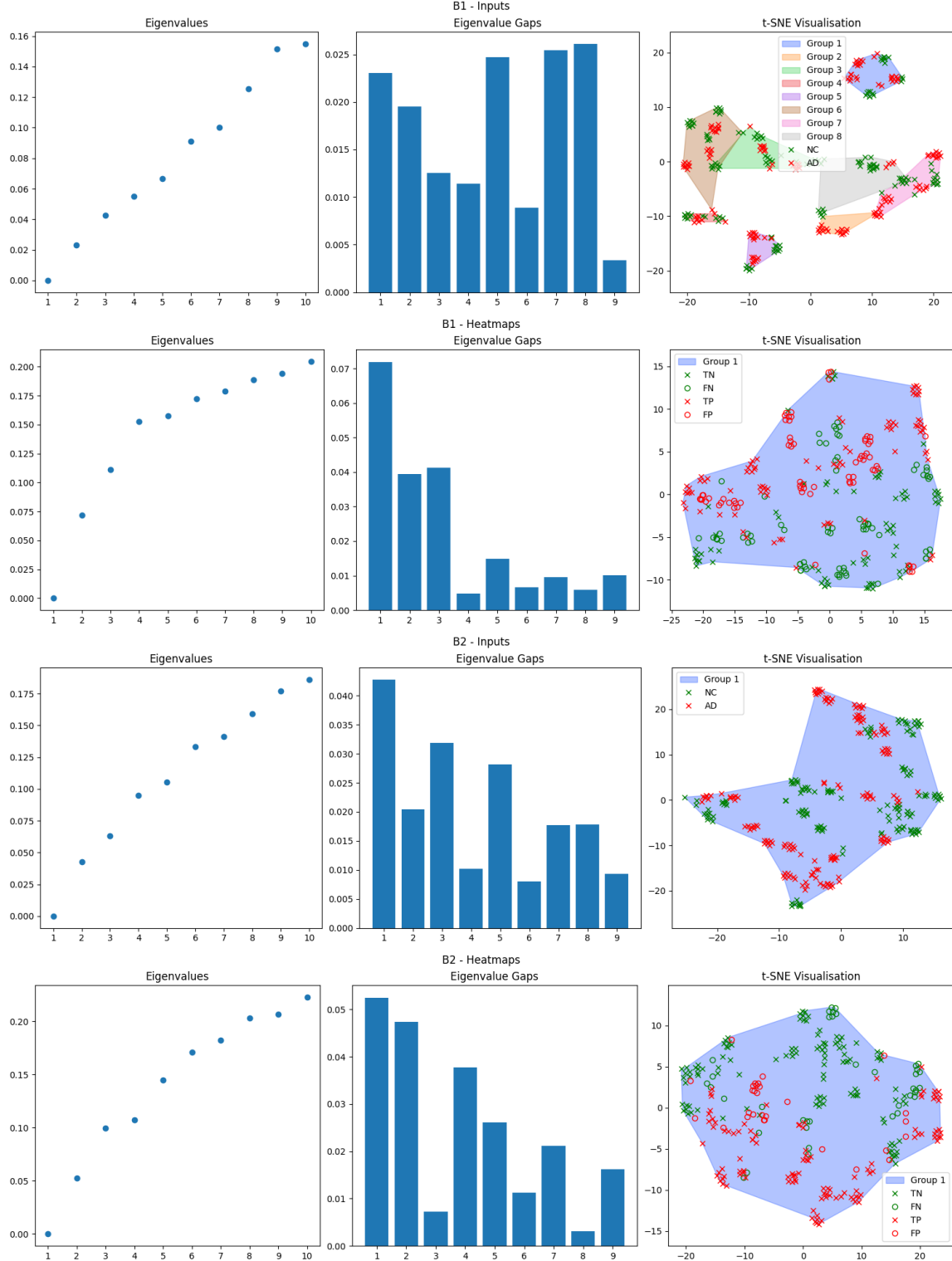


Fig. 12: Eigenvalues (column 1), the respective eigenvalue gaps (column 2) of the Laplacian matrix and the t-SNE visualization (column 3) of input (rows 1 and 3) and heatmap groupings (rows 2 and 4) for models B1 (aligned T1w MRI, 13.75% binarization) and B2 (skull-stripped T1w MRI, 13.75% binarization).

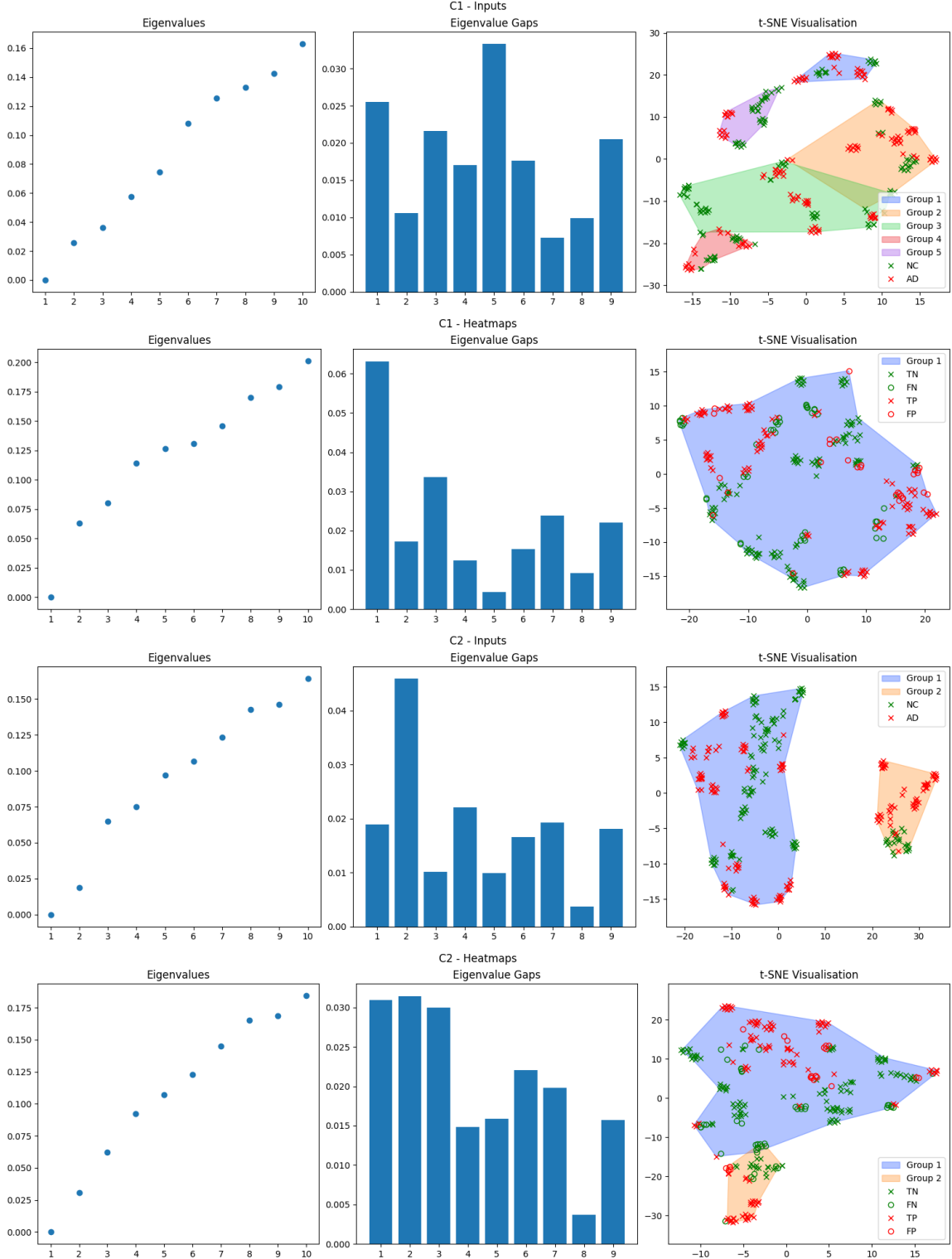


Fig. 13: Eigenvalues (column 1), the respective eigenvalue gaps (column 2) of the Laplacian matrix and the t-SNE visualization (column 3) of input (rows 1 and 3) and heatmap groupings (rows 2 and 4) for models C1 (aligned T1w MRI, 27.5% binarization) and C2 (skull-stripped T1w MRI, 27.5% binarization).

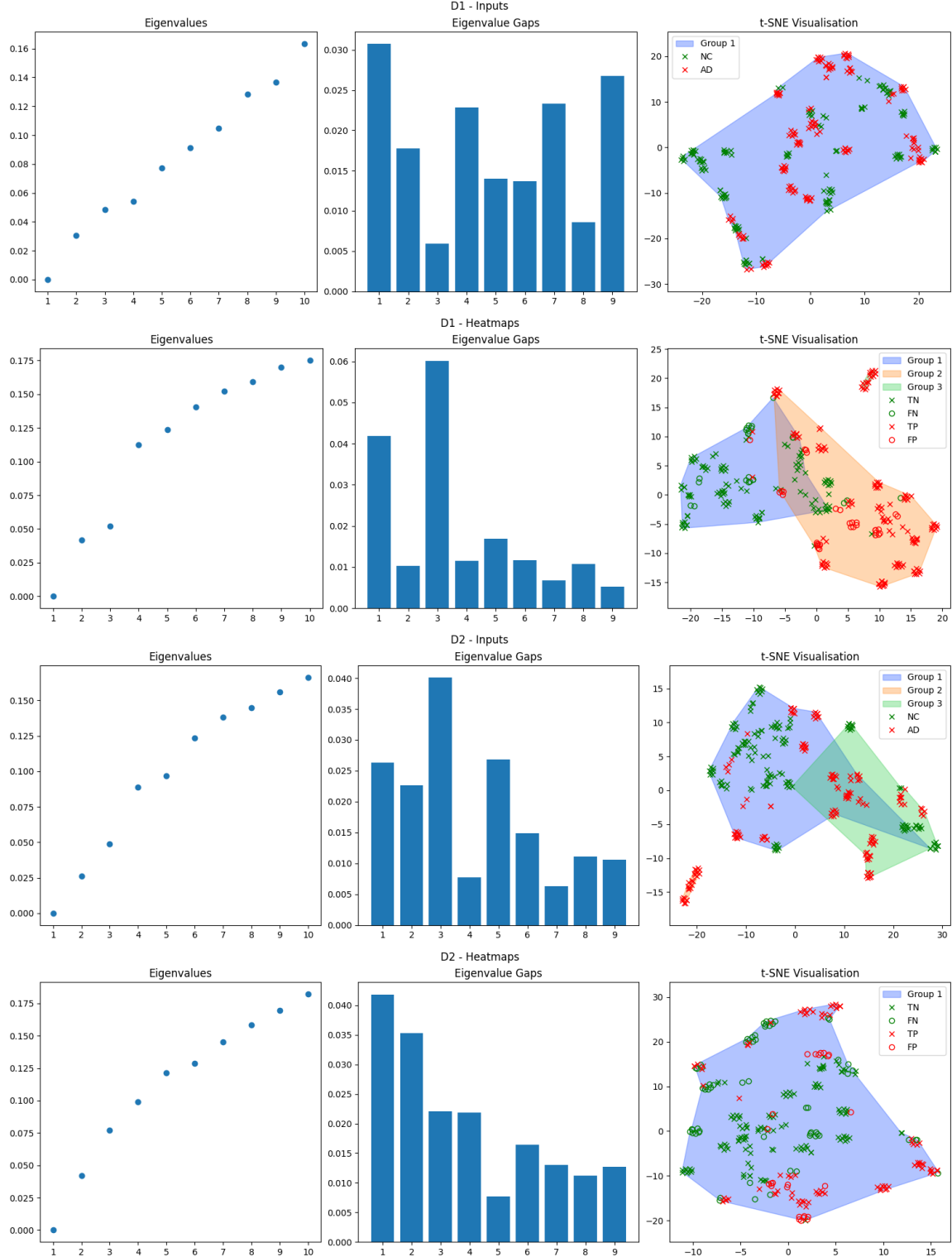


Fig. 14: Eigenvalues (column 1), the respective eigenvalue gaps (column 2) of the Laplacian matrix and the t-SNE visualization (column 3) of input (rows 1 and 3) and heatmap groupings (rows 2 and 4) for models D1 (aligned T1w MRI, 41.25% binarization) and D2 (skull-stripped T1w MRI, 41.25% binarization).

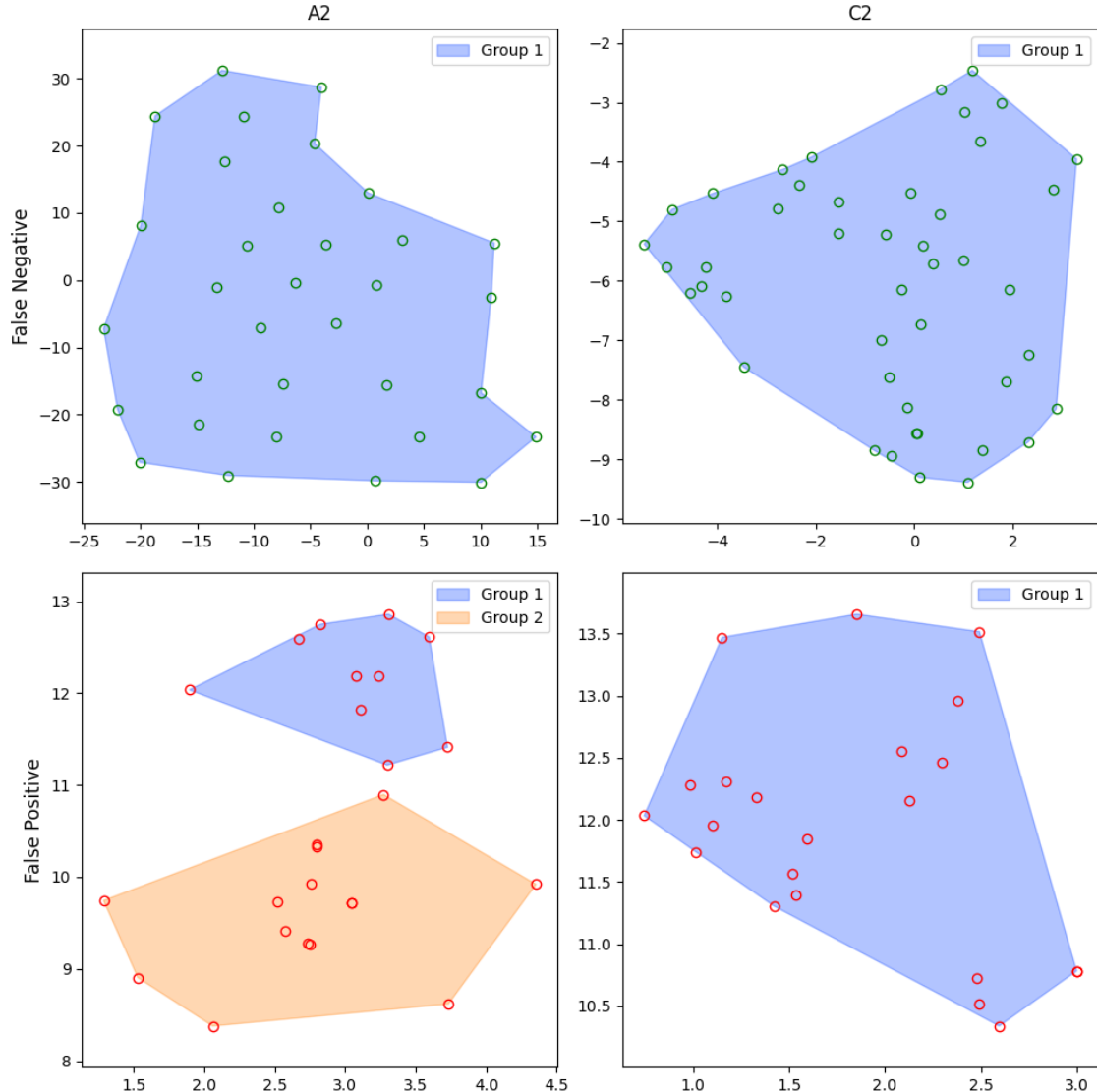


Fig. 15: t-SNE visualization of heatmaps for False Negative (row 1) and False Positive (row 2) samples in models A2 (reference) and C2 (27.5% binarization). Only the False Positive heatmaps of model A2 form two clusters, while all others group into one.

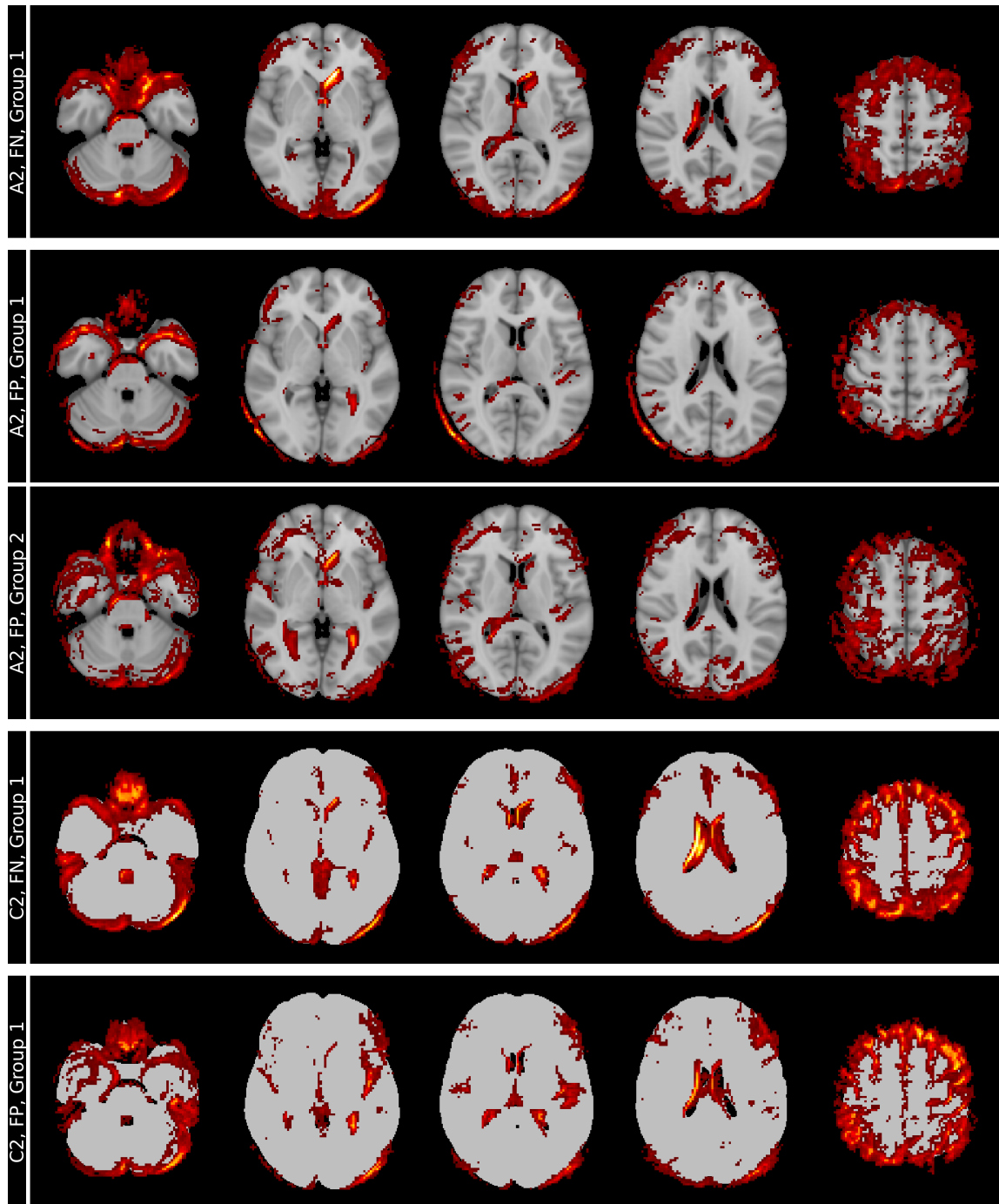


Fig. 16: Mean heatmaps from spectral clustering misclassified samples in models A2 and C2. In A2 (skull-stripping), False Negative (row 1, Group 1) and False Positive (row 2, Group 1) samples show distinct relevance in the temporal lobe (column 1), while False Positive samples in row 3 (Group 2) exhibit more pronounced ventricles (column 2). Model C2 also shows differences in the temporal lobes, ventricles, and cortex between False Negative and False Positive samples (row 4 vs row 5). Note: FN = False Negative, FP = False Positive.